

THE MID-INFRARED CONTINUA OF SEYFERT GALAXIES

RAJESH P. DEO¹, GORDON T. RICHARDS¹, D. M. CRENSHAW², AND S. B. KRAEMER³

¹ Department of Physics, Drexel University, 3141, Chestnut Street, Philadelphia, PA 19104-2816, USA; rpd@physics.drexel.edu, gtr@physics.drexel.edu

² Department of Physics and Astronomy, Georgia State University, Atlanta, GA 30303, USA; crenshaw@chara.gsu.edu

³ Catholic University of America, and the Exploration of the Universe Division, NASA's Goddard Space Flight Center, Code 667, Greenbelt, MD 20771, USA; kraemer@yancey.gsfc.nasa.gov

Received 2009 January 7; accepted 2009 September 3; published 2009 October 7

ABSTRACT

An analysis of archival mid-infrared (mid-IR) spectra of Seyfert galaxies from the *Spitzer Space Telescope* observations is presented. We characterize the nature of the mid-IR active nuclear continuum by subtracting a template starburst spectrum from the Seyfert spectra. The long wavelength part of the spectrum contains a strong contribution from the starburst-heated cool dust; this is used to effectively separate starburst-dominated Seyferts from those dominated by the active nuclear continuum. Within the latter category, the strength of the active nuclear continuum drops rapidly beyond $\sim 20 \mu\text{m}$. On average, type 2 Seyferts have weaker short-wavelength active nuclear continua as compared to type 1 Seyferts. Type 2 Seyferts can be divided into two types, those with strong polycyclic aromatic hydrocarbon (PAH) bands and those without. The latter type show polarized broad emission lines in their optical spectra. The PAH-dominated type 2 Seyferts and Seyfert 1.8/1.9s show very similar mid-IR spectra. However, after the subtraction of the starburst component, there is a striking similarity in the active nuclear continuum of all Seyfert optical types. PAH-dominated Seyfert 2s and Seyfert 1.8/1.9s tend to show weak active nuclear continua in general. A few type 2 Seyferts with weak/absent PAH bands show a bump in the spectrum between 15 and $20 \mu\text{m}$. We suggest that this bump is the peak of a warm ($\sim 200 \text{ K}$) blackbody dust emission, which becomes clearly visible when the short-wavelength continuum is weaker. This warm blackbody emission is also observed in other Seyfert optical subtypes, suggesting a common origin in these active galactic nuclei.

Key words: galaxies: active – galaxies: nuclei – galaxies: Seyfert – infrared: galaxies

Online-only material: color figures

1. INTRODUCTION

The complete mid-infrared (mid-IR) spectra of Seyfert galaxies (a class of active galactic nuclei (AGNs); Seyfert 1943) have been available only in recent past (e.g., Sturm et al. 2002; Verma et al. 2005; Weedman et al. 2005; Deo et al. 2007). Many *Spitzer* spectra of nearby Seyfert galaxies show a strong contribution from star-forming features in the form of polycyclic aromatic hydrocarbon (PAH) bands (e.g., Clavel et al. 2000; Buchanan et al. 2006; Tommasin et al. 2008). A number of these features, such as the $7.7 \mu\text{m}$ and the $17 \mu\text{m}$ PAH complex, are strongly blended with each other, complicating the estimation of the underlying active nuclear continuum. Further, the mid-IR opacity includes a strong contribution from the silicate bands at 10 and $18 \mu\text{m}$. Thus, estimating the intrinsic active nuclear continua in the mid-IR is a non-trivial task, with the primary hurdle being the subtraction of the starburst component.

Previous studies have hinted that the continuum in the $1\text{--}8 \mu\text{m}$ range is non-stellar in origin and is likely a result of thermal emission from dust heated close to sublimation temperature by the optical/ultraviolet continuum from the central source (Edelson & Malkan 1986; Alonso-Herrero et al. 2001; Imanishi & Alonso-Herrero 2004; Mushotzky et al. 2008). In a multi-wavelength photometric study of spectral energy distributions (SED) of predominantly radio-quiet Sloan Digital Sky Survey (SDSS) quasars, Richards et al. (2006) and Gallagher et al. (2007) noted that the $1\text{--}8 \mu\text{m}$ spectral index (α_ν) is strongly anti-correlated with infrared luminosity in type 1 quasars. The more luminous quasars have flatter $1\text{--}8 \mu\text{m}$ slopes. A linear correlation between the optical continuum luminosity and the infrared luminosity suggests that the observed bump around

$\sim 2.2 \mu\text{m}$ in the SED is driven by the dust re-emission. For example, the $2.2 \mu\text{m}$ bump is clearly visible in the near-IR spectrum of Mrk 1239 (Rodríguez-Ardila & Mazzalay 2006).

Due to the presence of strong PAH bands in the $5\text{--}8 \mu\text{m}$ range in many Seyfert spectra, direct measurement of the active nuclear continuum in this region is only possible in sources with very weak or absent PAH features. An alternative is to subtract the starburst contribution using a template starburst spectrum and then study the residual continuum. We take this simple approach in this paper. In Section 2, we describe our archival sample and the data analysis techniques. We discuss the observed mid-IR spectra in Section 3. In Section 4, we use simple continuum diagnostics that allows us to classify Seyfert mid-IR spectra into PAH-dominated and AGN-dominated groups and understand continuum properties. In Section 5, we discuss the starburst contribution in Seyfert spectra and the resulting continuum shapes after subtraction of the starburst template spectrum. In Section 6, we summarize our results.

2. SAMPLE SELECTION AND DATA ANALYSIS

We consider a sample of Seyfert galaxies derived from the *Spitzer Space Telescope* archives. This sample is listed in Table 1 with redshifts obtained from the NASA/IPAC Extragalactic Database⁴ (NED) along with the *Spitzer* archive numbers (AORKEY). We primarily use archival InfraRed Spectrograph (IRS; Houck et al. 2004) spectra extracted from programs 3069 (PI: J. Gallimore, mapping-mode spectra⁵), 3374 (PI: S. Kraemer, staring mode spectra) and Weedman et al. (2005;

⁴ <http://nedwww.ipac.caltech.edu/>

⁵ See: <http://ssc.spitzer.caltech.edu/documents/SOM/>.

Table 1
Observation Summary, Redshifts, Optical Seyfert Types, and Extraction Apertures

Galaxy	Redshift	Seyfert	<i>b/a</i>	<i>Spitzer</i>	Obs.	Extraction Rectangle			Parsec
Name		Type		AOR	Mode	R.A. (deg)	Decl. (deg)	Aperture (")	per arcsec
(1)	(2)	(3)	(4)	(5)	(6)	(7)	(8)	(9)	(10)
3C 226	0.817700	S1h	1.00	11298560	S	24655.19
3C 234	0.184800	S1h	1.00	11305728	S	4292.75
3C 265	0.811000	S1h	1.00	11299584	S	24406.85
3C 321	0.096100	S1h	0.70	10828544	S	2110.22
CGCG381-051	0.03067	H2	0.67	12483328	M	357.174904	2.237392	18.506x27.508	643.03
ESO 12-G21	0.030021	S1.5	0.22	12465920	M	10.178473	-79.235550	16.650x24.890	629.12
ESO 33-G2	0.01810	S2	0.82	12473088	M	74.014906	-75.539219	16.651x24.891	375.94
FSC 09104	0.442000	S1h	1.00	6619136	S	11694.26
IC 4329A	0.01605	S1.2	0.29	12480000	M	207.334737	-30.307954	12.957x18.319	332.84
IC 5063	0.011348	S1h	0.66	12465152	M	313.002802	-57.064322	25.401x35.919	234.49
IRAS 05189-2524	0.042563	S1h	0.96	4969216	S	900.21
IRASF 01475-0740	0.01767	S2	0.83	12474880	M	27.512248	-7.431963	14.799x22.275	366.89
IRASF 03450+0055	0.031000	S1.5	0.96	12455424	M	56.918450	1.084858	16.640x24.881	650.11
IRASF 04385-0828	0.01510	S2	0.50	12447232	M	70.229938	-8.374696	16.657x23.555	312.92
IRASF 15480-0344	0.03030	S2	0.84	12480256	M	237.676552	-3.886854	12.955x18.318	635.10
MCG+0-29-23	0.024897	S2	0.88	12443648	M	170.300469	-2.984643	14.801x19.668	519.76
MCG-03-34-064	0.016541	S1h	0.80	20367616	S	343.15
MCG-2-33-34	0.01463	S1n	0.58	12481280	M	193.056402	-13.413451	12.952x18.317	303.07
MCG-2-40-4	0.02519	S1	0.81	12481536	M	237.108125	-13.755182	14.804x22.282	525.99
MCG-2-8-39	0.02989	S2	0.69	12476928	M	45.129079	-11.417929	14.791x23.687	626.32
MCG-3-34-63	0.02133	S2	0.29	12477696	M	200.584610	-16.706397	16.651x22.278	444.10
MCG-3-58-7	0.03146	S1.9	0.80	12457984	M	342.405623	-19.275421	14.799x20.927	659.98
MCG-5-13-17	0.01264	S1.5	0.67	12468480	M	79.899175	-32.659368	12.947x18.308	261.45
MCG-6-30-15	0.00775	S2	0.60	12457472	M	203.980171	-34.293642	16.646x23.544	159.71
Mrk 1239	0.019927	S1n	0.38	12453120	M	148.079113	-1.612924	16.649x23.546	414.45
Mrk 3	0.013509	S1h	0.89	3753472	S	279.61
Mrk 334	0.02196	S1.8	0.70	10870016	S	457.44
Mrk 335	0.02578	S1.2	1.00	12476416	M	1.582227	20.201022	16.662x23.556	538.55
Mrk 348	0.01503	S1h	0.78	12472832	M	12.197642	31.954601	16.652x24.891	311.45
Mrk 463E	0.050000	S1h	1.00	4980736	S	1063.21
Mrk 471	0.03423	S1.8	0.67	10868992	S	719.56
Mrk 477	0.037726	S1h	0.71	17643008	S	795.09
Mrk 6	0.01881	S1.5	0.63	12483584	M	103.064183	74.431101	16.653x23.552	390.89
Mrk 609	0.03449	S1.8	0.90	10870528	S	725.17
Mrk 622	0.02323	S2	0.95	10869248	S	484.35
Mrk 704	0.029234	S1.2	0.57	12444416	M	139.607652	16.304607	18.497x26.162	612.27
Mrk 766	0.012929	S1.5	0.80	12465408	M	184.608565	29.814439	16.650x23.549	267.49
Mrk 79	0.02219	S1.2	0.52	12453632	M	115.635502	49.809536	16.651x24.887	462.31
Mrk 817	0.03145	S1.5	0.80	12461056	M	219.101248	58.795290	18.501x24.890	659.77
Mrk 883	0.03750	S1.9	0.62	10869504	S	790.20
Mrk 9	0.03987	S1.5	0.80	12483072	M	114.235533	58.770872	16.649x23.548	841.60
Mrk 938	0.01978	S2	0.36	12473856	M	2.778625	-12.109529	18.495x26.162	411.35
NGC 1056	0.00515	S2	0.48	12464896	M	40.701906	28.571643	16.653x23.548	105.92
NGC 1125	0.01093	S2	0.50	12454656	M	42.919692	-16.652879	18.501x26.167	225.78
NGC 1143/4	0.028847	S2	0.63	12448512	M	43.801754	-0.185407	18.498x24.888	603.99
NGC 1194	0.01360	S1.9	0.48	12472064	M	45.955575	-1.105563	14.802x22.279	281.51
NGC 1241	0.01351	S2	0.61	12468224	M	47.812412	-8.924313	18.500x27.500	279.63
NGC 1320	0.00888	S2	0.32	12454400	M	51.203760	-3.044172	16.659x23.551	183.15
NGC 1365	0.005457	S1.8	0.55	12480768	M	53.402894	-36.143278	20.354x30.120	112.26
NGC 1386	0.002895	S2	0.38	12474112	M	54.195896	-35.994983	16.653x22.280	59.44
NGC 1667	0.01517	S2	0.78	12459520	M	72.155696	-6.323982	24.049x41.076	314.38
NGC 2273	0.006138	S1h	0.78	4851712	S	126.33
NGC 2622	0.02862	S1.8	0.50	10869760	S	599.14
NGC 2639	0.01113	S3	0.61	12477440	M	130.906163	50.203587	24.045x42.587	229.95
NGC 2992	0.007710	S1.9	0.31	12478208	M	146.424140	-14.327517	20.342x27.495	158.88
NGC 3079	0.00372	S2	0.18	12475136	M	150.502129	55.682721	20.352x31.506	76.42
NGC 3081	0.007976	S1h	0.76	18509824	S	164.39
NGC 3227	0.00386	S1.5	0.67	12450304	M	155.875181	19.871115	20.323x36.634	79.31
NGC 3511	0.003699	S1	0.34	12473600	M	165.848750	-23.089783	24.050x38.136	75.99
NGC 3516	0.00884	S1.5	0.76	12473344	M	166.716783	72.571111	18.499x26.162	182.32
NGC 3660	0.012285	S2	0.81	12477184	M	170.883777	-8.658924	16.647x23.541	254.04
NGC 3786	0.00893	S1.8	0.59	10871808	S	184.19
NGC 3982	0.00370	S1.9	0.88	12449536	M	179.130254	55.128503	24.054x32.734	76.01
NGC 4051	0.00234	S1n	0.75	12451072	M	180.797723	44.533906	18.503x27.506	48.02

Table 1
(Continued)

Galaxy Name (1)	Redshift (2)	Seyfert Type (3)	b/a (4)	<i>Spitzer</i> AOR (5)	Obs. Mode (6)	Extraction Rectangle			Parsec per arcsec (10)
						R.A. (deg) (7)	Decl. (deg) (8)	Aperture (") (9)	
NGC 4151	0.00332	S1.5	0.71	12470784	M	182.642569	39.408036	16.648x24.887	68.18
NGC 424	0.01166	S1h	0.44	12444160	M	17.867777	-38.085092	20.347x28.774	241.00
NGC 4388	0.008419	S1h	0.19	12460288	M	186.443590	12.662449	20.347x28.778	173.58
NGC 4501	0.007609	S2	0.54	12445440	M	187.994494	14.420342	20.351x30.112	156.78
NGC 4507	0.011801	S1h	0.76	18511104	S	243.94
NGC 4579	0.00507	S3b	0.80	12462080	M	189.439250	11.821549	24.051x36.721	104.26
NGC 4593	0.009000	S1.0	0.74	12457216	M	189.913681	-5.344758	16.652x23.546	185.64
NGC 4594	0.003416	S1.9	0.40	12456960	M	189.997069	-11.623687	16.648x23.545	70.16
NGC 4602	0.00847	S1.9	0.35	12465664	M	190.161835	-5.127129	24.043x42.585	174.64
NGC 4922 NED01	0.023860	S2	0.79	12477952	M	195.349342	29.317079	25.406x43.701	497.72
NGC 4941	0.00370	S2	0.53	12471552	M	196.052465	-5.542940	25.400x47.925	76.01
NGC 4968	0.00986	S2	0.47	12464128	M	196.781667	-23.674650	20.352x27.507	203.52
NGC 5005	0.00316	S3b	0.48	12475648	M	197.741665	37.061589	18.499x24.887	64.89
NGC 513	0.01954	S1.9	0.43	12467712	M	21.112954	33.797022	20.350x28.780	406.29
NGC 5135	0.013693	S2	0.67	12445696	M	201.439919	-29.831243	18.495x27.497	283.46
NGC 5256 NED01	0.027600	S2	0.75	12459264	M	204.581404	48.278533	20.353x30.119	577.35
NGC 526A	0.01910	S1.9	0.53	12454912	M	20.987415	-35.061446	25.401x47.921	397.01
NGC 5347	0.00779	S2	0.76	12481792	M	208.329504	33.492829	14.798x22.273	160.54
NGC 5506	0.006181	S1i	0.24	12453888	M	213.317594	-3.205489	18.499x24.891	127.22
NGC 5548	0.01717	S1.5	0.93	12481024	S	356.37
NGC 5929	0.00831	S3	0.78	12444928	M	231.531375	41.672728	14.803x20.931	171.32
NGC 5953	0.00656	S2	0.81	12476160	M	233.641348	15.196836	20.346x30.113	135.06
NGC 6810	0.006775	S2	0.28	12479488	M	295.901492	-58.651454	18.498x26.161	139.51
NGC 6860	0.014884	S1.5	0.62	12462592	M	302.204152	-61.095376	20.347x30.111	308.39
NGC 6890	0.008069	S1.9	0.80	12452608	M	304.580525	-44.802776	18.497x27.499	166.32
NGC 7130	0.01615	S1.9	0.93	12463616	M	327.082844	-34.953547	16.652x24.889	334.94
NGC 7172	0.00868	S2	0.56	12450048	M	330.515750	-31.867704	25.400x39.675	179.00
NGC 7213	0.005839	S3b	0.90	12449024	M	332.323337	-47.161801	20.348x27.500	120.15
NGC 7314	0.00476	S1.9	0.46	12469504	M	338.950394	-26.048111	25.397x39.677	97.87
NGC 7469	0.01632	S1.5	0.73	12472320	M	345.815619	8.871944	16.648x22.273	338.51
NGC 7496	0.00550	S2	0.91	12462336	M	347.449971	-43.430211	20.352x30.114	113.14
NGC 7582	0.005254	S1	0.42	12445184	M	349.601583	-42.364982	20.349x28.777	108.06
NGC 7590	0.005255	S2	0.37	12482560	M	349.731754	-42.233643	18.498x26.163	108.08
NGC 7603	0.02952	S1.5	0.67	12450816	M	349.737435	0.241247	20.352x30.116	618.39
NGC 7674	0.02892	S1h	0.91	12468736	M	351.987312	8.776636	18.501x27.500	605.55
NGC 788	0.013603	S1h	0.74	18944512	S	281.57
NGC 931	0.01665	S1.0	0.21	12460032	M	37.060954	31.309135	18.500x26.163	345.44
SDSS J1039+6430	0.401776	S1h	1.00	13630208	S	10444.00
SDSS J1641+3858	0.595835	S1h	0.86	13630464	S	16742.90
TOL 1238-364	0.01092	S1h	0.88	12466432	M	190.226517	-36.754040	16.654x23.549	225.58
UGC 11680 NED01	0.025988	S2	0.80	12459008	M	316.924025	3.868699	18.504x26.167	542.97
UGC 12138	0.02497	S1.8	0.88	10871296	S	521.31
UGC 7064	0.02500	S1.9	0.90	12467456	M	181.186346	31.179312	16.661x23.556	521.95
UM 146	0.01741	S1.9	0.77	10871040	S	361.42
WIR-IRAS 23060+0505	0.173000	S1h	1.00	4374528	S	3990.25

Notes. Col. (1): Galaxy name; Col. (2): Redshift, obtained from NASA Extragalactic Database (NED); Col. (3): Seyfert type from Véron-Cetty & Véron (2006)—S1: Seyfert 1 optical spectrum; S1h: broad polarized Balmer lines detected; S1i: broad Paschen lines observed in the infrared; S1n: narrow-line Seyfert 1; S1.0, S1.2, S1.5, S1.8, and S1.9: intermediate Seyfert galaxies (Note: In this paper, we consider S1.0–1.5 to be broadly Seyfert 1s in all analysis.); S2: Seyfert 2 spectrum; S3: LINER; S3b: LINER with broad Balmer lines; S3h: LINER with broad polarized Balmer lines detected; H2: nuclear H II region; Col. (4): Axial ratio, minor-to-major axis ratio of host galaxy obtained from NED, for host galaxies where b/a was not available we assumed it to be 1; Col. (5): *Spitzer* archive Astronomical Observation Request (AOR) number; Col. (6): Observing mode for *Spitzer/IRS* spectrum—S: staring mode, M: mapping mode; Cols. (7 and 8): Extraction rectangle for mapping-mode spectra: R.A. and Decl. of center-point in degrees; Col. (9): Extraction aperture in arcseconds. Col. (10): Radial extent in parsecs per arcsecond of the extraction aperture for the galaxy.

Mrk 3, low-resolution staring mode spectrum). Deo et al. (2007) presented single slit extractions of spectra from above-mentioned programs for about half of the current sample. During the initial work on that paper, CUBISM software was not yet available (Smith et al. 2007a). In this paper, we expand that sample and consider the complete IRS mapping-mode data sets from program 3069 along with other archival data sets now

available. This sample was chosen due to its large size and good sampling of different Seyfert optical types. We also test if the use of complete mapping-mode spectra leads to changes in the short-wavelength continuum. After the initial analysis, we noted that our sample lacked type 2 Seyferts with detected polarized broad emission lines. So, we added 16 Seyfert 2s selected from the compilation of Tran (2003) for which low-resolution IRS

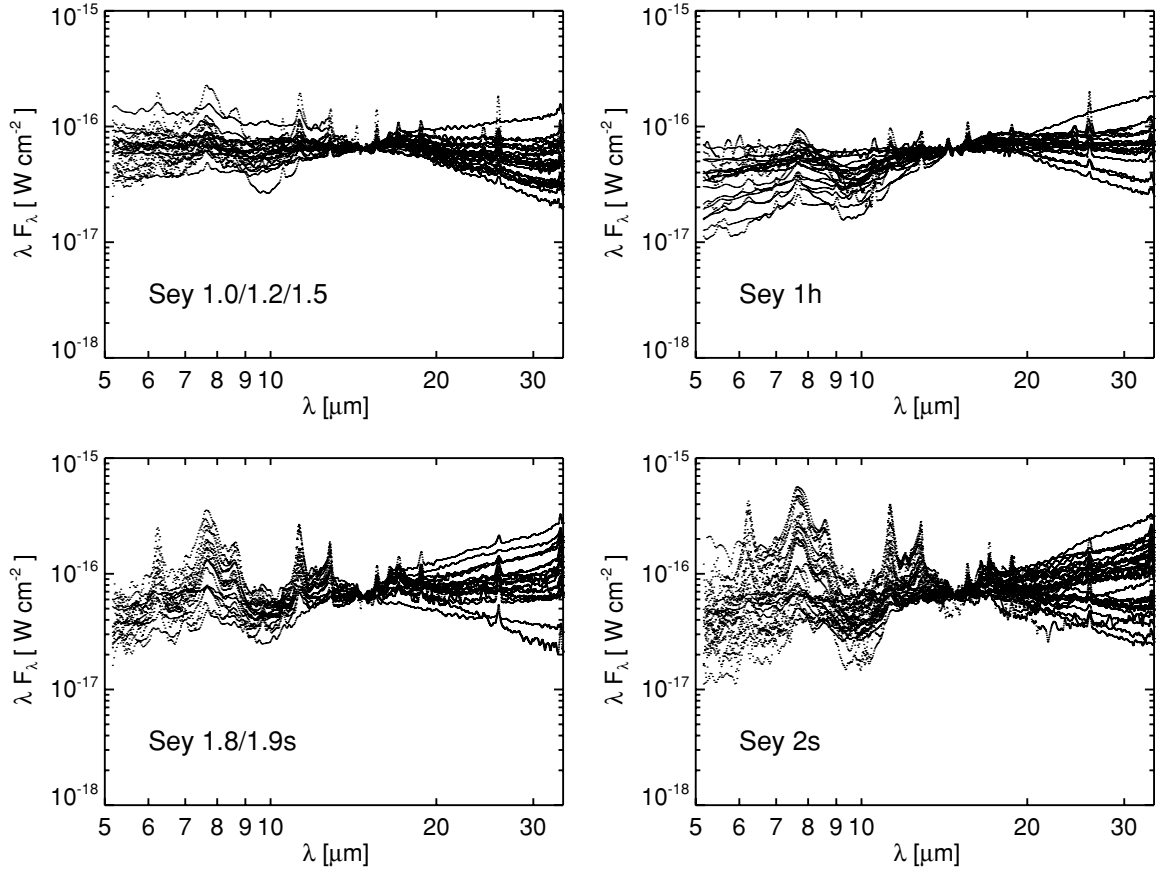


Figure 1. Mid-infrared spectra of the entire sample normalized at $14.7 \mu\text{m}$. Top left: Seyfert 1s; top right: Seyfert 2s with evidence of broad optical emission lines in polarized light; bottom left: Seyfert 1.8/1.9s spectra dominated by PAH features; bottom right: Seyfert 2 spectra dominated by PAH features. The short-wavelength continuum of PAH-weak type 2 Seyferts (top right) is on average weaker and steeper than type 1 Seyferts (top left). Seyfert 1.8/1.9s and PAH-strong type 2 Seyferts (bottom right) show very similar spectra.

spectra are available from the archive. These objects come from a number of different programs and their AOR numbers are listed in Table 1. Further, we obtained optical Seyfert classifications from the compilation of Véron-Cetty & Véron (2006; VCV hereafter) and host galaxy minor-to-major axis ratios (b/a) from NED. These are listed in Table 1. This paper contains a sample of 109 Seyfert galaxies with low-resolution IRS spectra.

The mapping-mode observations were reduced as below. From the low-resolution basic calibrated data (BCD) spectral images (for short-low, SL, and long-low, LL, modules), we built three-dimensional spectral cubes (two spatial (x , y) and one wavelength (z) dimension) using the CUBISM software package (Smith et al. 2007a). We wrote interactive data language (IDL) routines to script internal CUBISM routines to automate the reduction of spectral cubes. The pixel backtracking facility available within CUBISM was used to clean the cubes of bad pixels. One-dimensional spectra were extracted from these cubes using a common rectangular aperture for all four modules. These extraction apertures (see Table 1, Column 9) were selected to encompass as small a region as possible in the LL1 module without introducing pixel-aliasing effects in the extracted one-dimensional LL1 spectra. We note an increase in the absolute SL flux density values as compared to single slit extractions. This is expected due to the different pixel scales of the SL and LL modules and the larger aperture area as compared to a single slit. The extracted one-dimensional spectra were then imported into the SMART software package (Higdon et al. 2004) to normalize the separate modules. In most cases, no multiplicative shifts were necessary due to matched aperture extractions. When

corrections were necessary, the correction factor was always less than 10%. The ends of the spectral orders were clipped to remove data points affected by the reduced spectral response. The spectra were then re-binned to a common wavelength grid.

The staring-mode spectra were extracted as below. We started with BCD products obtained from the *Spitzer* archive. We median-combined multiple data collection event (DCE) image files into one image per module, order, and nod position. We differenced images from opposite orders to remove the sky background and then extracted spectra using the tapered-column extraction option within SMART. For cases, when differencing opposite orders was not possible, we used opposite nod positions. All the image and spectrum extraction operations were carried out inside SMART. The extracted spectra were cleaned by removing deviant data points and normalizing the spectra from different modules to form the complete mid-IR spectrum. Figure 1 shows the complete mid-IR spectra grouped according to their Seyfert types from Table 1.

We measured the mid-IR continuum at 5.5 , 10 , 14.7 , 20 , and $30 \mu\text{m}$, averaging within a window of $1 \mu\text{m}$, on the rest-frame spectra. These specific spectral regions were chosen to minimize the contribution from emission lines or PAH bands, thus primarily sampling the mid-IR continuum. We also measured the optical depth at $9.7 \mu\text{m}$. The silicate strength commonly quoted in *Spitzer* studies is $S_{9.7} = \ln(f_\lambda/f_c)$, which translates to $-\tau_{9.7}$ in our case. We follow the convention that negative optical depth implies a silicate emission feature. The peaks of these emission features typically occur around $10.5 \mu\text{m}$. We present optical depth as measured at $9.7 \mu\text{m}$ for

such sources. The continuum and optical depth measurements are given in Table 2. We also measured the equivalent widths and fluxes of PAH bands and the narrow emission lines. In this paper, we restrict ourselves only to continuum and optical depth measurements.

In all figures ahead, Seyfert 1s (including 1.2s and 1.5s) are represented by filled circles (types S1, S1.0, S1.2, and S1.5 from VCV). Seyfert 2s with broad emission lines detected in their polarized optical spectra (type S1h in VCV; and called hidden broad-line region, HBLR, in Tran 2003) are represented by filled diamond symbols. Seyfert 2s with undetected broad emission lines in their polarized optical spectra (type S2 from VCV, and called non-HBLR in Tran 2003) are represented with open squares. Seyfert 1.8/1.9s are represented with open triangles (S1.8 and S1.9 from VCV). Galaxies classified as LINER (type S3 from VCV) are represented by cross symbols. Each figure includes legends describing all Seyfert optical subtypes mentioned here.

3. THE MID-IR SPECTRA

Complete mid-IR spectra of the sample are presented in Figure 1. The top left panel shows type 1 Seyfert spectra. The top right panel shows type 2 Seyferts with broad-line region (BLR) detected in polarized light (e.g., Antonucci & Miller 1985; Tran 2003). The bottom left panel shows Seyfert 1.8/1.9s; these spectra are dominated by starburst-related PAH emission. These nuclei are likely weak emitters with a dominant contribution from circum-nuclear starbursts (Deo et al. 2007). The bottom right panel shows type 2 Seyferts with dominant starburst contribution (strong PAH bands). Clearly, the mid-IR spectra of Seyfert 1.8/1.9s are very similar to these type 2 Seyferts. Polarized broad emission lines have not yet been detected in these PAH-dominated type 2 Seyferts. This suggests that the starburst contribution from the host galaxy dominates over the active nuclear continuum in these sources. One of the goals of this study is to understand if these starburst-dominated nuclei have similar mid-IR continuum properties as starburst-weak type 1 and type 2 nuclei.

Examination of the spectra in Figure 1 shows that on average, the continuum is similar between all four classes. PAH-weak type 2 spectra (top right) show weaker and steeper short-wavelength continuum than PAH-weak type 1 spectra (top left) which are flatter. This is a direct evidence that short-wavelength mid-IR emission is absorbed to a certain degree in type 2 objects by the intervening dust torus.

Previous research work (e.g., Edelson & Malkan 1986; Rodriguez Espinosa et al. 1996; Klaas et al. 2001; Schweitzer et al. 2006) has suggested that the mid-IR SED is likely composed of three thermal components: hot (~ 1000 K), warm (~ 200 K), and cold (~ 60 K) dust emissions. This is reflected in the *IRAS* 25 and 60 μm photometry with the active nuclear SED being “warm” compared to the “cool” starbursts.

Almost all spectra show a curious emission peak/bump between 15 and 20 μm . This emission should not be confused with the silicate 18 μm peak (which is always much weaker than the 10 μm peak) or the 17 μm PAH complex. The feature is broad and the peak wavelength varies between 15 and 20 μm . This bump is observed most clearly in the top right panel of Figure 1 (S1h sources), as the short-wavelength continuum is weak in these sources. The presence of this feature in many other spectra (some with strong PAH contributions also) suggests a common origin in most Seyfert subtypes.

In Figure 2, we subtract the spectrum of Mrk 335 (a Seyfert 1.2) from the starburst-subtracted spectrum⁶ of Mrk 766 (a Seyfert 1.5). The Mrk 335 spectrum is a power-law-like spectrum with no hint of the 15–20 μm bump. The residual Mrk 766 spectrum shows the 15–20 μm bump. We compare the residual spectrum to the Mrk 3 (type 2, S1h) spectrum. Both spectra are almost identical. This suggests that the 15–20 μm bump is only visible when the power-law-like hot dust component is being absorbed, as in type 2 sources. Thus, it seems that the continuum shape of the mid-IR AGN spectrum depends on which of the three hot, warm, and cold components is brighter than others. In type 1 spectra, the hot component dominates; in type 2 spectra, the warm component dominates; while starburst-dominated objects show an excess of cold dust emission.

4. THE OBSERVED MID-IR CONTINUUM

Figure 3 shows a plot of spectral indices for all galaxies in the sample. Here, the spectral index⁷ is defined as

$$\alpha_{\lambda_1-\lambda_2} = \log_{10}(f_{\lambda_1}/f_{\lambda_2})/\log_{10}(\lambda_1/\lambda_2), \quad (1)$$

where f_{λ_1} is the flux density in $\text{W cm}^{-2} \mu\text{m}^{-1}$ and wavelengths are in μm . The dotted lines at $\alpha_{\lambda}(5.5-14.7) = -0.5$ and $\alpha_{\lambda}(20-30) = -0.5$ divide the figure in four quadrants. Three important conclusions can be drawn from this comparison: (1) most HBLR Seyfert 2s (class S1h in Table 1) are in the left quadrants; (2) most Seyfert 1s are in the bottom left quadrant; and (3) PAH-dominated Seyferts (some non-HBLR Seyfert 2s and Seyfert 1.8/1.9s) lie mostly in the right quadrants. Positive values of $\alpha_{\lambda}(20-30)$ indicate red and steep long-wavelength continua and a stronger contribution from cold ($T \sim 50-80$ K) thermal dust components (see the bottom panels of Figure 1). This cold component is likely associated with star formation (Klaas et al. 2001; Schweitzer et al. 2006). In the discussions that follow, we propose that the mid-IR spectra contain contribution from at least three thermal components: (1) a high temperature ($T \sim 500-1200$ K) “hot” component dominating at shorter wavelengths, (2) a “warm” component ($T \sim 200$ K) dominating at 15–20 μm , and (3) a “cool” component ($T \sim 50-80$ K) associated with star formation as mentioned above.

The arrows in Figure 3 represent how the spectral shape changes from one quadrant to another. Positive values of $\alpha_{\lambda}(5.5-14.7)$ suggest a dominance of warm ($T \sim 200$ K) thermal components and relatively steep short-wavelength continua in F_{λ} . Objects that will fall in this quadrant will show enhanced 15–20 μm bump in the mid-IR spectra. This emission bump is likely due to a warm thermal component peaking at these wavelengths. We would like to clarify that this is not the 18 μm silicate feature, but rather a thermal-modified blackbody (dust) emission underneath it, the short-wavelength side of which is clearly visible only when the short-wavelength continuum is weak. No object with the 15–20 μm bump as the dominant feature in the mid-IR spectrum shows 10 μm in emission; this suggests that the short-wavelength continuum due to the hot component and any associated silicate emission features is being absorbed.

As the emission of the hot dust component increases, the spectra begin to show a power-law-like flattening at short wavelengths: $\alpha_{\lambda}(5.5-14.7)$ becomes more negative and the dominance of the warm thermal continuum decreases. This

⁶ See Section 5 ahead for details of the starburst subtraction process.

⁷ The wavelength index α_{λ} and the frequency index α_{ν} are related by $\alpha_{\nu} = -(\alpha_{\lambda} + 2)$.

Table 2
Continuum Flux Densities and Apparent Optical Depth at 9.7 μm

Galaxy Name (1)	Continuum Flux Density (Jy)					Optical Depth (7)
	5.5 μm (2)	10 μm (3)	14.7 μm (4)	20 μm (5)	30 μm (6)	
3C 226	3.82E-03 (4.37E-04)	4.73E-03 (9.31E-04)	1.57E-02 (1.02E-03)	2.03E-02 (1.98E-03)	...	0.6175
3C 234	5.25E-02 (4.35E-03)	1.34E-01 (6.46E-03)	2.21E-01 (3.47E-03)	2.67E-01 (3.02E-03)	2.66E-01 (6.53E-03)	-0.0106
3C 265	6.66E-03 (1.50E-03)	1.06E-02 (1.19E-03)	1.61E-02 (1.08E-03)	-0.1688
3C 321	1.19E-02 (1.42E-03)	3.28E-02 (5.12E-03)	1.78E-01 (1.53E-02)	2.71E-01 (1.37E-02)	5.15E-01 (2.16E-02)	0.6349
CGCG381-051	8.73E-02 (6.20E-02)	1.24E-01 (1.13E-02)	1.93E-01 (6.00E-03)	3.62E-01 (1.65E-02)	5.51E-01 (8.89E-03)	-0.1339
ESO 12-G21	6.02E-02 (1.45E-02)	1.14E-01 (7.53E-03)	1.40E-01 (5.46E-03)	1.64E-01 (6.74E-03)	2.55E-01 (3.20E-03)	-0.1241
ESO 33-G2	8.98E-02 (1.84E-02)	1.89E-01 (1.69E-02)	3.11E-01 (7.48E-03)	3.56E-01 (9.98E-03)	3.16E-01 (4.86E-03)	-0.0620
FSC 09104	5.98E-02 (6.92E-03)	1.35E-01 (1.40E-02)	2.75E-01 (4.12E-03)	3.70E-01 (4.78E-03)	...	0.2929
IC 4329A	5.53E-01 (2.30E-02)	9.81E-01 (6.17E-02)	1.60E+00 (3.99E-02)	1.91E+00 (4.48E-02)	1.52E+00 (1.36E-02)	-0.0520
IC 5063	2.18E+00 (3.19E-02)	3.02E+00 (3.37E-02)	3.89E+00 (6.16E-02)	...
IRAS 05189-2524	2.04E-01 (1.35E-02)	3.95E-01 (3.12E-02)	1.16E+00 (1.91E-02)	2.01E+00 (1.29E-01)	5.91E+00 (1.32E-01)	0.3367
IRASF 01475-0740	4.46E-02 (1.10E-02)	1.61E-01 (1.57E-02)	2.61E-01 (1.03E-02)	4.37E-01 (2.00E-02)	4.81E-01 (7.02E-03)	-0.1827
IRASF 03450+0055	1.39E-01 (8.77E-03)	2.65E-01 (1.48E-02)	3.47E-01 (5.59E-03)	4.57E-01 (1.54E-02)	3.87E-01 (1.22E-02)	-0.1850
IRASF 04385-0828	2.27E-01 (1.45E-02)	2.38E-01 (1.85E-02)	8.02E-01 (2.88E-02)	1.07E+00 (2.24E-02)	1.46E+00 (2.50E-02)	0.7856
IRASF 15480-0344	4.29E-02 (9.36E-03)	1.53E-01 (2.09E-02)	2.99E-01 (1.86E-02)	4.22E-01 (5.74E-03)	4.92E-01 (8.65E-03)	-0.0815
MCG+0-29-23	6.69E-02 (2.04E-02)	1.01E-01 (6.78E-03)	2.48E-01 (6.52E-03)	3.83E-01 (8.24E-03)	8.54E-01 (1.75E-02)	0.0629
MCG-03-34-064	1.75E-01 (2.53E-02)	5.04E-01 (6.26E-02)	1.39E+00 (5.68E-02)	2.05E+00 (1.39E-02)	2.95E+00 (5.14E-02)	0.2911
MCG-2-33-34	2.74E-02 (6.77E-03)	6.44E-02 (1.87E-02)	1.12E-01 (1.90E-02)	1.59E-01 (3.64E-03)	2.31E-01 (6.59E-03)	-0.0590
MCG-2-40-4	2.02E-01 (1.89E-02)	3.27E-01 (1.62E-02)	5.45E-01 (1.93E-02)	6.78E-01 (1.34E-02)	9.53E-01 (1.19E-02)	0.1155
MCG-2-8-39	3.12E-02 (8.95E-03)	1.21E-01 (1.09E-02)	2.53E-01 (7.18E-03)	2.92E-01 (1.61E-02)	2.92E-01 (3.33E-03)	-0.0427
MCG-3-34-63	1.13E-02 (8.81E-03)	1.61E-02 (5.04E-03)	2.31E-02 (3.59E-03)	4.08E-02 (6.41E-03)	1.01E-01 (3.51E-03)	-0.0420
MCG-3-58-7	1.47E-01 (8.75E-03)	2.78E-01 (1.13E-02)	4.76E-01 (1.21E-02)	7.01E-01 (2.02E-02)	9.38E-01 (1.45E-02)	-0.0072
MCG-5-13-17	5.27E-02 (1.13E-02)	1.11E-01 (9.16E-03)	2.10E-01 (4.28E-03)	3.19E-01 (4.38E-03)	4.19E-01 (5.80E-03)	0.1221
MCG-6-30-15	1.80E-01 (1.34E-02)	3.34E-01 (2.20E-02)	4.80E-01 (8.65E-03)	6.45E-01 (1.05E-02)	6.10E-01 (6.27E-03)	-0.0771
Mrk 1239	4.57E-01 (1.60E-02)	7.29E-01 (2.24E-02)	8.85E-01 (2.70E-02)	1.03E+00 (3.31E-02)	9.14E-01 (1.42E-02)	-0.0910
Mrk 3	1.02E-01 (1.12E-02)	2.94E-01 (4.24E-02)	1.25E+00 (7.25E-02)	2.07E+00 (2.26E-02)	2.36E+00 (2.27E-02)	0.3461
Mrk 334	4.81E-02 (7.58E-03)	1.13E-01 (7.10E-03)	2.52E-01 (9.27E-03)	5.71E-01 (2.39E-02)	1.36E+00 (4.01E-02)	0.2496
Mrk 335	1.44E-01 (1.28E-02)	2.03E-01 (1.28E-02)	2.53E-01 (9.50E-03)	2.80E-01 (9.27E-03)	2.62E-01 (2.92E-03)	-0.1258
Mrk 348	1.25E-01 (1.41E-02)	1.88E-01 (1.69E-02)	4.30E-01 (1.79E-02)	5.67E-01 (1.51E-02)	4.95E-01 (5.85E-03)	0.3455
Mrk 463E	2.47E-01 (1.42E-02)	3.30E-01 (3.13E-02)	8.39E-01 (2.08E-02)	1.28E+00 (1.53E-02)	1.54E+00 (1.44E-02)	0.3582
Mrk 471	7.44E-03 (1.59E-03)	1.58E-02 (1.15E-03)	2.69E-02 (2.13E-03)	4.31E-02 (3.01E-03)	9.11E-02 (3.88E-03)	0.1419
Mrk 477	2.44E-02 (3.23E-03)	7.46E-02 (9.39E-03)	2.31E-01 (1.34E-02)	4.21E-01 (5.48E-03)	6.18E-01 (6.51E-03)	0.2195

Table 2
(Continued)

Galaxy Name	Continuum Flux Density (Jy)					Optical Depth
	5.5 μm	10 μm	14.7 μm	20 μm	30 μm	
(1)	(2)	(3)	(4)	(5)	(6)	(7)
Mrk 609	1.76E−02 (5.24E−03)	4.52E−02 (2.70E−03)	9.80E−02 (6.13E−03)	1.80E−01 (7.76E−03)	4.35E−01 (9.05E−03)	0.3291
Mrk 6	1.45E−01 (1.02E−02)	2.08E−01 (1.73E−02)	3.72E−01 (1.72E−02)	5.37E−01 (1.80E−02)	4.98E−01 (8.54E−03)	−0.0280
Mrk 622	7.80E−03 (1.54E−03)	3.78E−02 (3.40E−03)	1.06E−01 (6.61E−03)	2.55E−01 (8.40E−03)	5.51E−01 (5.31E−03)	0.1071
Mrk 704	1.91E−01 (2.05E−02)	3.54E−01 (1.90E−02)	5.05E−01 (9.12E−03)	5.22E−01 (1.85E−02)	4.02E−01 (6.29E−03)	−0.0163
Mrk 766	1.49E−01 (1.62E−02)	3.02E−01 (2.41E−02)	6.95E−01 (2.73E−02)	1.02E+00 (8.78E−03)	1.38E+00 (2.56E−02)	0.1533
Mrk 79	1.77E−01 (1.58E−02)	2.98E−01 (1.47E−02)	4.66E−01 (1.78E−02)	5.98E−01 (1.04E−02)	6.91E−01 (9.23E−03)	−0.0141
Mrk 817	1.23E−01 (2.39E−02)	2.91E−01 (2.17E−02)	4.79E−01 (2.37E−02)	8.08E−01 (3.47E−02)	1.13E+00 (1.31E−02)	−0.0577
Mrk 883	5.80E−03 (1.26E−03)	1.67E−02 (2.41E−03)	4.49E−02 (1.62E−03)	1.18E−01 (7.17E−03)	3.03E−01 (7.93E−03)	0.1741
Mrk 9	1.04E−01 (1.92E−02)	1.92E−01 (1.21E−02)	2.62E−01 (6.06E−03)	3.42E−01 (7.71E−03)	3.91E−01 (7.69E−03)	0.0281
Mrk 938	1.15E−01 (3.16E−02)	9.93E−02 (1.64E−02)	4.99E−01 (1.48E−02)	1.08E+00 (6.44E−02)	4.02E+00 (1.36E−01)	1.0488
NGC 1056	6.46E−02 (2.09E−02)	1.11E−01 (1.07E−02)	1.54E−01 (1.90E−02)	2.33E−01 (6.18E−03)	5.45E−01 (1.29E−02)	−0.0326
NGC 1125	4.71E−02 (1.18E−02)	5.65E−02 (1.26E−02)	2.72E−01 (1.79E−02)	4.95E−01 (1.23E−02)	1.08E+00 (2.18E−02)	0.9306
NGC 1143/4	7.79E−02 (2.40E−02)	8.75E−02 (1.34E−02)	1.85E−01 (1.20E−02)	0.4689
NGC 1194	1.52E−01 (1.47E−02)	1.18E−01 (1.45E−02)	4.03E−01 (8.76E−03)	4.10E−01 (7.86E−03)	4.72E−01 (5.43E−03)	0.9308
NGC 1241	3.15E−02 (1.64E−02)	4.78E−02 (1.21E−02)	1.05E−01 (5.17E−03)	1.58E−01 (5.66E−03)	2.98E−01 (6.42E−03)	0.3753
NGC 1320	1.44E−01 (1.65E−02)	3.11E−01 (2.21E−02)	5.61E−01 (1.53E−02)	7.84E−01 (1.04E−02)	9.40E−01 (1.24E−02)	0.0757
NGC 1365	7.29E−01 (1.26E−01)	1.23E+00 (7.41E−02)	2.69E+00 (1.28E−01)	4.89E+00 (1.18E−01)	1.23E+01 (3.43E−01)	0.2823
NGC 1386	2.03E−01 (1.50E−02)	2.89E−01 (3.41E−02)	8.44E−01 (3.92E−02)	1.03E+00 (1.86E−02)	1.58E+00 (2.96E−02)	0.5700
NGC 1667	7.56E−02 (3.61E−02)	1.36E−01 (1.07E−02)	2.24E−01 (1.15E−02)	3.04E−01 (1.66E−02)	6.67E−01 (1.94E−02)	0.0048
NGC 2273	1.19E−01 (1.42E−02)	2.10E−01 (1.60E−02)	5.54E−01 (1.16E−02)	8.58E−01 (1.69E−02)	1.69E+00 (3.03E−02)	0.3614
NGC 2622	8.54E−03 (8.38E−04)	2.19E−02 (2.41E−03)	5.41E−02 (3.07E−03)	8.32E−02 (1.41E−03)	1.02E−01 (1.18E−03)	0.0899
NGC 2639	5.99E−02 (2.11E−02)	5.75E−02 (1.51E−02)	8.29E−02 (8.20E−03)	1.20E−01 (1.87E−02)	1.99E−01 (1.12E−02)	0.2610
NGC 2992	1.89E−01 (2.67E−02)	3.87E−01 (4.50E−02)	8.14E−01 (2.86E−02)	1.03E+00 (1.21E−02)	1.50E+00 (3.51E−02)	0.2296
NGC 3079	3.33E−01 (7.64E−02)	2.38E−01 (3.93E−02)	7.11E−01 (7.85E−02)	7.11E−01 (3.76E−02)	3.36E+00 (1.45E−01)	1.0463
NGC 3081	5.28E−02 (6.55E−03)	1.74E−01 (2.56E−02)	5.11E−01 (3.69E−02)	7.95E−01 (5.34E−03)	1.09E+00 (8.37E−03)	0.0953
NGC 3227	7.22E−01 (2.88E−02)	1.22E+00 (3.15E−02)	1.76E+00 (3.96E−02)	...
NGC 3511	6.37E−02 (2.21E−02)	8.39E−02 (1.46E−02)	1.37E−01 (1.44E−02)	1.72E−01 (8.91E−03)	3.46E−01 (1.43E−02)	0.1253
NGC 3516	1.97E−01 (1.27E−02)	3.11E−01 (2.37E−02)	4.80E−01 (1.45E−02)	6.97E−01 (7.83E−03)	7.77E−01 (1.28E−02)	0.0365
NGC 3660	...	3.14E−02 (7.34E−03)	4.48E−02 (3.92E−03)	9.01E−02 (8.20E−03)	1.70E−01 (5.21E−03)	0.6161
NGC 3786	2.69E−02 (3.23E−03)	4.85E−02 (4.80E−03)	8.95E−02 (4.20E−03)	1.43E−01 (4.45E−03)	3.00E−01 (6.09E−03)	0.1110
NGC 3982	6.43E−02 (2.51E−02)	1.28E−01 (1.65E−02)	2.03E−01 (5.24E−03)	3.37E−01 (1.23E−02)	6.56E−01 (1.70E−02)	0.0014
NGC 4051	2.11E−01 (1.60E−02)	4.61E−01 (2.23E−02)	7.72E−01 (1.59E−02)	1.10E+00 (1.85E−02)	1.24E+00 (1.24E−02)	0.0769

Table 2
(Continued)

Galaxy Name	Continuum Flux Density (Jy)					Optical Depth
(1)	5.5 μ m (2)	10 μ m (3)	14.7 μ m (4)	20 μ m (5)	30 μ m (6)	9.7 μ m (7)
NGC 4151	6.80E-01 (2.83E-02)	1.56E+00 (1.22E-01)	3.16E+00 (7.85E-02)	4.55E+00 (9.77E-02)	3.64E+00 (3.89E-02)	-0.0464
NGC 424	5.28E-01 (2.50E-02)	9.06E-01 (4.59E-02)	1.38E+00 (4.90E-02)	1.63E+00 (3.80E-02)	1.28E+00 (1.19E-02)	-0.0307
NGC 4388	2.29E-01 (2.46E-02)	2.90E-01 (6.73E-02)	1.06E+00 (6.28E-02)	1.80E+00 (4.66E-02)	2.80E+00 (4.83E-02)	0.7792
NGC 4501	1.15E-01 (1.56E-02)	9.98E-02 (1.88E-02)	1.16E-01 (5.89E-03)	1.16E-01 (1.82E-02)	1.38E-01 (5.66E-03)	0.4831
NGC 4507	2.11E-01 (1.47E-02)	4.71E-01 (4.04E-02)	8.63E-01 (2.41E-02)	1.28E+00 (5.48E-03)	1.71E+00 (3.23E-02)	0.0848
NGC 4579	1.31E-01 (1.46E-02)	1.62E-01 (4.21E-02)	1.24E-01 (1.79E-02)	-0.3803
NGC 4593	2.22E-01 (1.42E-02)	4.25E-01 (1.50E-02)	5.43E-01 (1.30E-02)	6.64E-01 (1.47E-02)	8.13E-01 (1.18E-02)	-0.0721
NGC 4594	2.43E-01 (1.74E-02)	1.36E-01 (7.20E-03)	8.21E-02 (8.00E-03)	-0.3486
NGC 4602	4.78E-02 (1.57E-02)	8.32E-02 (1.19E-02)	1.20E-01 (1.05E-02)	1.75E-01 (1.05E-02)	3.65E-01 (1.30E-02)	-0.0254
NGC 4922 NED01	1.61E-01 (3.98E-02)	3.40E-01 (5.47E-02)	8.56E-01 (6.60E-02)	0.5302
NGC 4941	1.62E-01 (1.13E-02)	2.99E-01 (2.11E-02)	4.50E-01 (1.30E-02)	...
NGC 4968	1.03E-01 (2.13E-02)	2.49E-01 (3.09E-02)	6.21E-01 (2.95E-02)	9.32E-01 (2.00E-02)	1.02E+00 (1.77E-02)	0.3205
NGC 5005	1.81E-01 (1.65E-02)	1.59E-01 (3.35E-02)	2.25E-01 (1.23E-02)	2.85E-01 (1.42E-02)	9.08E-01 (3.66E-02)	0.6118
NGC 513	4.97E-02 (1.68E-02)	9.63E-02 (1.06E-02)	1.36E-01 (7.21E-03)	1.98E-01 (1.00E-02)	3.30E-01 (1.17E-02)	0.1337
NGC 5135	1.51E-01 (3.08E-02)	2.62E-01 (3.16E-02)	6.70E-01 (3.61E-02)	1.31E+00 (3.52E-02)	3.03E+00 (8.45E-02)	0.3971
NGC 5256 NED01	5.85E-02 (1.47E-02)	7.62E-02 (1.69E-02)	2.56E-01 (2.22E-02)	4.95E-01 (2.58E-02)	1.37E+00 (2.67E-02)	0.5591
NGC 526A	3.08E-01 (1.35E-02)	3.87E-01 (1.23E-02)	2.55E-01 (1.23E-02)	...
NGC 5347	6.19E-02 (8.71E-03)	2.10E-01 (1.92E-02)	5.22E-01 (1.22E-02)	7.86E-01 (1.78E-02)	7.91E-01 (1.03E-02)	0.0025
NGC 5506	9.33E-01 (2.17E-02)	6.88E-01 (1.06E-01)	2.18E+00 (6.61E-02)	2.86E+00 (5.59E-02)	4.05E+00 (6.38E-02)	0.7640
NGC 5929	1.35E-02 (7.60E-03)	2.08E-02 (7.60E-03)	2.89E-02 (2.66E-03)	5.84E-02 (3.46E-03)	1.13E-01 (3.62E-03)	0.0243
NGC 5953	1.20E-01 (3.57E-02)	1.87E-01 (1.81E-02)	3.16E-01 (3.25E-02)	5.14E-01 (1.47E-02)	1.27E+00 (3.37E-02)	0.0941
NGC 6810	2.02E-01 (4.37E-02)	4.13E-01 (2.65E-02)	9.59E-01 (2.85E-02)	2.13E+00 (2.86E-02)	3.33E+00 (7.18E-02)	0.2068
NGC 6860	1.64E-01 (1.28E-02)	2.48E-01 (5.12E-03)	3.25E-01 (1.26E-02)	3.87E-01 (1.16E-02)	3.36E-01 (4.73E-03)	-0.0012
NGC 6890	8.02E-02 (1.55E-02)	1.49E-01 (1.10E-02)	2.62E-01 (8.16E-03)	3.98E-01 (1.08E-02)	5.79E-01 (9.52E-03)	-0.0208
NGC 7130	9.29E-02 (1.67E-02)	2.05E-01 (1.62E-02)	5.38E-01 (2.21E-02)	1.08E+00 (3.30E-02)	2.47E+00 (6.89E-02)	0.2710
NGC 7172	4.20E-01 (3.05E-02)	3.89E-01 (2.41E-02)	9.81E-01 (2.94E-02)	...
NGC 7213	1.79E-01 (1.62E-02)	4.14E-01 (2.80E-02)	4.87E-01 (1.59E-02)	7.33E-01 (2.00E-02)	5.77E-01 (1.68E-02)	-0.2470
NGC 7314	2.23E-01 (2.10E-02)	2.71E-01 (1.46E-02)	4.36E-01 (7.01E-03)	...
NGC 7469	3.31E-01 (4.74E-02)	7.67E-01 (4.89E-02)	1.65E+00 (4.61E-02)	3.28E+00 (1.04E-01)	6.11E+00 (1.67E-01)	0.1045
NGC 7496	4.71E-02 (1.41E-02)	1.37E-01 (1.53E-02)	3.77E-01 (1.85E-02)	8.96E-01 (2.54E-02)	2.14E+00 (5.02E-02)	0.1744
NGC 7582	6.34E-01 (5.33E-02)	5.79E-01 (7.27E-02)	1.97E+00 (8.92E-02)	3.52E+00 (1.22E-01)	9.33E+00 (2.74E-01)	0.8284
NGC 7590	4.44E-02 (1.32E-02)	6.55E-02 (8.10E-03)	8.54E-02 (6.82E-03)	1.20E-01 (5.80E-03)	2.46E-01 (1.17E-02)	-0.0658

Table 2
(Continued)

Galaxy Name (1)	Continuum Flux Density (Jy)					Optical Depth (7)
	5.5 μm (2)	10 μm (3)	14.7 μm (4)	20 μm (5)	30 μm (6)	
NGC 7603	2.39E-01 (1.25E-02)	3.31E-01 (6.28E-03)	2.98E-01 (1.41E-02)	3.06E-01 (1.11E-02)	3.12E-01 (6.83E-03)	-0.0630
NGC 7674	1.89E-01 (2.60E-02)	3.89E-01 (3.44E-02)	9.24E-01 (3.37E-02)	1.37E+00 (2.31E-02)	1.83E+00 (1.57E-02)	0.2811
NGC 788	3.01E-02 (3.30E-03)	8.23E-02 (1.05E-02)	2.16E-01 (7.87E-03)	3.01E-01 (1.34E-03)	3.47E-01 (3.59E-03)	0.1234
NGC 931	2.22E-01 (1.81E-02)	3.99E-01 (2.04E-02)	6.56E-01 (2.67E-02)	8.79E-01 (1.40E-02)	9.29E-01 (9.02E-03)	0.0166
SDSS J1039+6430	6.74E-03 (2.00E-04)	1.33E-02 (1.17E-03)	2.72E-02 (7.75E-04)	-0.0103
SDSS J1641+3858	3.75E-03 (1.02E-03)	2.13E-02 (2.20E-03)	-0.0473
TOL 1238-364	1.18E-01 (1.90E-02)	3.36E-01 (3.82E-02)	9.20E-01 (3.69E-02)	1.67E+00 (1.58E-02)	2.16E+00 (3.93E-02)	0.2025
UGC 11680 NED01	3.62E-02 (6.71E-03)	8.87E-02 (1.54E-02)	1.33E-01 (7.37E-03)	1.80E-01 (1.12E-02)	2.11E-01 (6.44E-03)	0.0946
UGC 12138	2.43E-02 (2.07E-03)	5.56E-02 (5.07E-03)	1.11E-01 (5.79E-03)	1.79E-01 (3.68E-03)	3.03E-01 (1.09E-02)	0.2383
UGC 7064	3.06E-02 (1.36E-02)	8.51E-02 (6.15E-03)	1.52E-01 (6.79E-03)	2.31E-01 (1.16E-02)	3.28E-01 (5.85E-03)	0.1045
UM 146	6.76E-03 (8.04E-04)	1.42E-02 (1.05E-03)	3.22E-02 (1.62E-03)	5.29E-02 (3.55E-03)	9.72E-02 (5.13E-04)	0.2348
WIR-IRAS 23060+0505	1.01E-01 (6.50E-03)	1.58E-01 (9.47E-03)	3.31E-01 (4.01E-03)	4.53E-01 (1.27E-02)	7.51E-01 (1.46E-02)	0.3170

Notes. Col. (1): Galaxy name; Cols. (2–6): Continuum flux density as measured on the spectrum at 5.5, 10., 14.7, 20, and 30 μm in Jansky; Col. (7): Observed optical depth (apparent) at 9.7 μm ; 1σ errors are given in parenthesis.

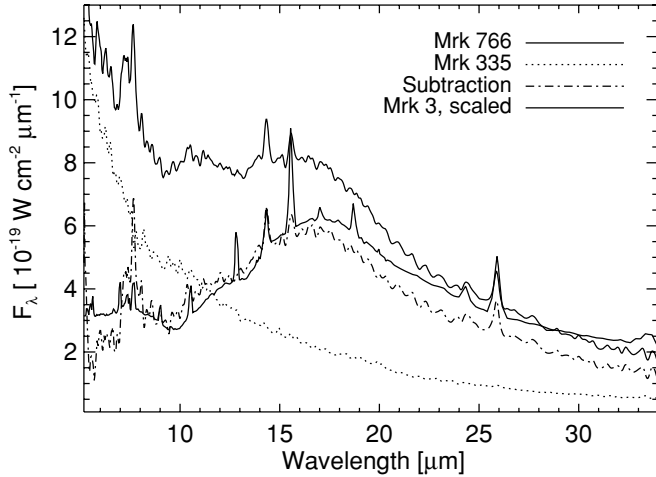


Figure 2. Subtraction of Mrk 335 (type 1) spectrum from the spectrum of Mrk 766 (type 1, starburst-subtracted, see Section 5). The residual spectrum is very similar to the Mrk 3 (type 2) spectrum and shows the prominent 15–20 μm bump. The spectra are displayed in the same order at 10 μm as is indicated in the legend.

power law is likely the Rayleigh–Jean’s tail of the hot component with dust close to its sublimation temperature. At any point along this type 2 to type 1 sequence, adding a cold dust component to the spectrum shifts the spectrum toward positive (steep) $\alpha_\lambda(20\text{--}30)$. NGC 7469, a Seyfert 1.5 with strong starburst contribution is identified in Figure 3. Beyond this point in the right quadrants, we see that there are no Seyfert 1s and the region with $\alpha_\lambda(20\text{--}30) \gtrsim -0.5$ is mostly populated by Seyfert 1.8/1.9s and Seyfert 2s with undetected polarized broad emission lines. In these galaxies, the AGN continuum

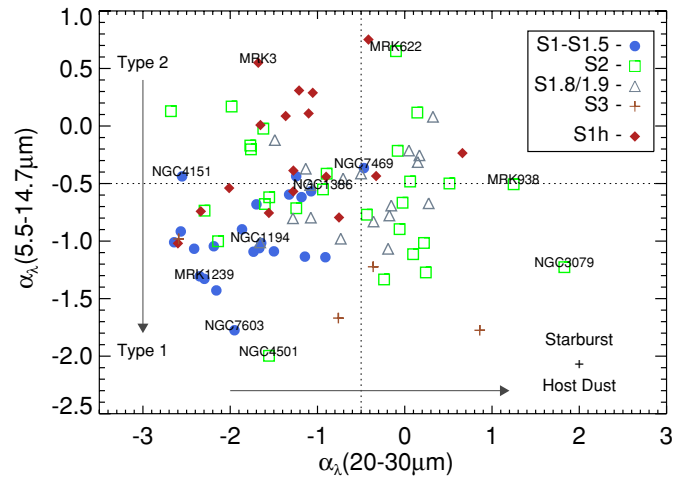


Figure 3. Mid-IR continua of Seyfert Galaxies: Seyfert 2s with hidden broad-line regions (S1h) are represented as filled diamond symbols, Seyfert 1s (including 1.2s and 1.5s) are filled circles, Seyfert 1.8/1.9s are open triangles, and Seyfert 2s with undetected polarized broad emission lines are open squares. Liners are represented with cross symbols. As $\alpha_\lambda(20\text{--}30 \mu\text{m})$ increases, spectra contain more starburst contribution; as $\alpha_\lambda(5.5\text{--}14.7 \mu\text{m})$ varies from 0.5 to -2.0 , spectra are more dominated by the hot dust component due to the active nucleus. The arrows indicate how the spectral shape changes from type 2 to type 1 Seyferts (see also Figure 7); and along this sequence, addition of a cold starburst component of increasing strength moves the source position to the right in the figure. The dotted lines show rough division between different Seyfert types. See Section 4 for further discussion.

(A color version of this figure is available in the online journal.)

contribution is weaker than the contribution from the circum-nuclear starburst in the host galaxy (Deo et al. 2007). The spectra are primarily dominated by PAH features and very

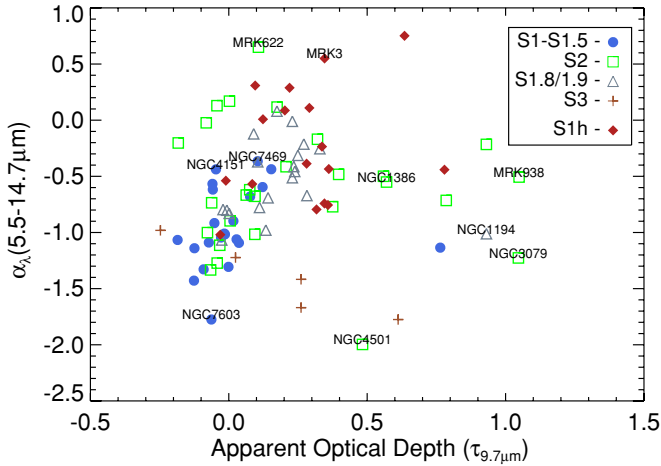


Figure 4. There is a weak correlation between apparent optical depth ($\tau_{9.7}$) and $\alpha_\lambda(5.5-14.7 \mu\text{m})$ providing general support for inclination dependence in AGN models. Some sources show large apparent silicate optical depth ($\tau_{9.7} \sim 1$): these have highly inclined host galaxy disks (see Table 1). For sources with $\tau_{9.7} \gtrsim 0.4$ silicate absorption is primarily due to cold dust in the host galaxy. (A color version of this figure is available in the online journal.)

red long-wavelength continua. Mrk 938 and NGC 3079 show very red long-wavelength continua in our sample, and both of these galaxies are highly inclined to our line of sight (see Table 1), their continua are dominated by the emission from the cold dust. The relatively steep short-wavelength continua of these starburst-dominated Seyferts indicate that continuum measurements at $5.5 \mu\text{m}$ include a contribution from nearby $6.2 \mu\text{m}$ PAH complex.

Figure 4 compares the apparent silicate optical depth at $9.7 \mu\text{m}$ ($\tau_{9.7}$) with $\alpha_\lambda(5.5-14.7)$. We find a weak correlation between $\tau_{9.7}$ and $\alpha_\lambda(5.5-14.7)$. For $\tau_{9.7} \leq 0.4$, we find a Spearman rank correlation, $\rho = 0.46$ with $P_{\text{null}} = 1.85 \times 10^{-5}$. This suggests that as the inclination of observer's line of sight changes from pole-on for type 1 objects to edge-on for type 2 objects, the inner hot dust is obscured, in agreement with the unified models (Antonucci 1993). This result is in agreement with trends noted by Hao et al. (2007) between continuum colors and silicate strength.

Measurement of optical depth requires defining a continuum which is a subjective process, leading to large errors in measured values of optical depths. We generate the continuum by fitting a spline curve through certain pivot points. As mentioned above, pivots at 5.5 , 14.7 , 20 , and $30 \mu\text{m}$ are used. Apart from these pivots, we also use additional points around 8 and $12 \mu\text{m}$ to define the blue and red ends of the silicate absorption feature. The process is very similar to the one presented in Figure 2 of Spoon et al. (2007) and should produce identical results in most cases. As a test, in Figure 5, we present a comparison between the $11.3 \mu\text{m}$ PAH equivalent width and the optical depth. The absence of any correlation in the figure suggests that we are not biasing our continuum placements when strong PAH bands are present in the spectra. Thus, our optical depth measurements should be fairly accurate in most cases.

A few objects in Figure 4 do not follow this trend and show strong silicate optical depths $\tau_{9.7} > 0.5$. In all such objects, the strong silicate absorption is a result of absorption due to dust in the host galaxy rather than in the immediate vicinity of the central source. This conclusion is supported by objects that show very red long-wavelength continua (NGC 3079 and

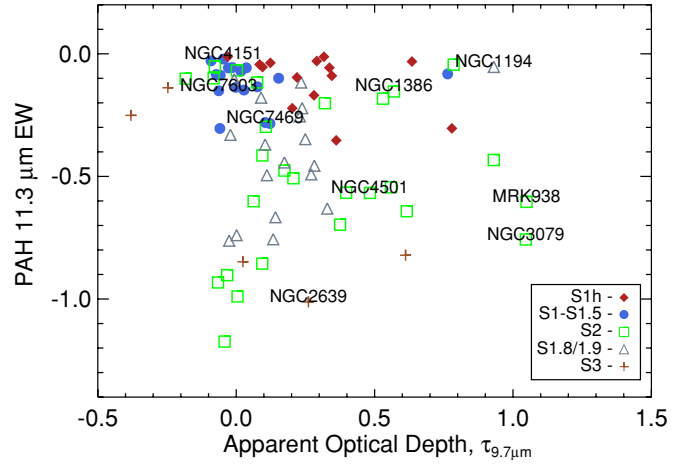


Figure 5. There is no correlation between the equivalent width of the $11.3 \mu\text{m}$ PAH band and the measured apparent optical depth at $9.7 \mu\text{m}$, suggesting that the presence of strong PAH bands does not bias our continuum placement in the short-wavelength region of the mid-IR spectra, where defining the continuum is highly subjective due to the presence of blended PAH emission bands, and silicate and ice absorption features. (A color version of this figure is available in the online journal.)

Mrk 938). To investigate the dependence of $\tau_{9.7}$ on the inclination of the host galaxy, we plotted $\tau_{9.7}$ against the b/a of the host galaxy. This comparison is shown in Figure 6, which indicates that for $b/a < 0.5$, dust in the host galaxy disk can contribute significantly to the observed silicate absorption and the long-wavelength continuum. A few high-inclination galaxies (e.g., IC4329A) do not show silicate absorption, but rather silicate emission. We checked *Hubble Space Telescope* images of IC4329A and note that the narrow-line region of this object is clearly visible in the F533N (narrow-band optical filter around [O III] $\lambda 5007$) filter above the inclined host galaxy disk. Our line of sight to the central source in IC4329A likely does not intersect any dense dust clouds in the host interstellar medium. An alternative explanation, when our line of sight is not close to the polar axis of the ionization bicone in an inclined host galaxy disk, could be that clumpy distributions can produce weak silicate emission features, or very weak absorption by filling in the existing absorption. In summary, the host interstellar medium can have substantial effect on the mid-IR nuclear continuum and a clear indication of this is a very red long-wavelength continuum in the mid-IR spectrum of an inclined disk galaxy. A comparison of $\alpha_\lambda(5.5-14.7)$ with $\tau_{9.7}$ for objects with $b/a > 0.5$ preserves the correlation in Figure 4, suggesting that the observed correlation is probing dust obscuration closer to the central source than on kilo-parsec scales.

The effects of the host galaxy ISM on AGN mid-IR spectra are demonstrated in Figure 7, where we plot representative mid-IR spectra around the silicate optical depth ($\tau_{9.7}$) versus $\alpha_\lambda(5.5-14.7 \mu\text{m})$ plot from Figure 4. On the left-hand side, as the $\alpha_\lambda(5.5-14.7)$ increases from -2.0 to 1.0 , the short-wavelength continuum is gradually suppressed, and we progress from strong type 1 source (bottom left) dominating the short-wavelength mid-IR to strong type 2 source (top left) peaking between 15 and $20 \mu\text{m}$. The left-hand side panels show the true behavior of mid-IR active nuclear continua without contribution from external host galaxy features. As the apparent optical depth increases above 0.5 , the spectra show stronger contribution from dust in the host galaxy, and enhanced PAH features (top right and bottom right in Figure 4). NGC 1194 (left, middle box in

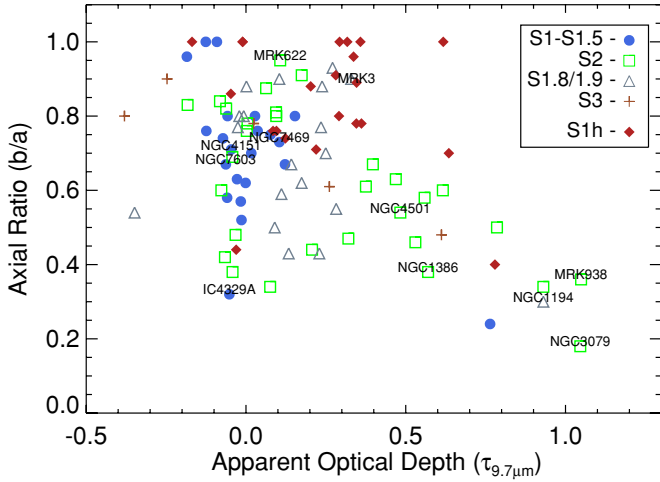


Figure 6. Correlation between the optical depth of $9.7 \mu\text{m}$ silicate feature and the ratio of minor-to-major axis (b/a) of the host galaxy. The b/a values are taken from the NASA/IPAC Extragalactic Database. Objects for which b/a could not be estimated are assumed to have $b/a = 1$.

(A color version of this figure is available in the online journal.)

Figure 7) lacks these starburst features, but shows one of the strongest silicate absorption features at both 10 and $18 \mu\text{m}$. Figures 6 and 7 validate the observation that many Seyfert galaxies with highly inclined host galaxy disks are classified as type 2 or type 1.8/1.9s (Keel 1980; Maiolino & Rieke 1995).

These results imply that to study effects of dust in the torus, we need to look at sources with $-0.3 \lesssim \tau_{9.7} \lesssim 0.3$ and $\alpha_{\lambda}(20-30) \lesssim -0.5$. A key property that distinguishes active nuclear continua is the similarity of $\alpha_{\lambda}(20-30)$ for both type 1 and type 2 Seyferts (see Figure 1), and the fact that the $20-30 \mu\text{m}$ continua are bluer than the star formation dominated very red continua. For type 1.5 and type 2 Seyferts (S1h), the dominant $15-20 \mu\text{m}$ feature suggests that the dust structures responsible for these features are warm ($T \sim 200$ K), and the spectral index in the $20-30 \mu\text{m}$ is decided by the slope of the Rayleigh–Jean’s tail of this warm component. As can be seen from the top left panels in Figure 7, the short-wavelength continua are significantly weaker in type 2 sources as compared to type 1 sources (bottom left). In the $20-30 \mu\text{m}$ region of the spectrum, the differences are smaller in agreement with previous observation by Buchanan et al. (2006).

4.1. Non-HBLR Seyferts and Starburst Contributions

Based on the spectro-polarimetry survey of the CfA and the $12 \mu\text{m}$ sample of Seyfert galaxies, Tran (2001, 2003) suggested that there are two different populations of Seyfert galaxies: (1) type 2 Seyferts that host a HBLR (S1h in Table 1), and hence are intrinsically identical to a type 1 Seyfert; and (2) type 2 Seyferts that show no signatures of the BLR in spectro-polarimetry (non-HBLR) and have optical narrow-line ratios weaker than the HBLRs on the Baldwin–Phillip–Terlevich (BPT) diagram (Veilleux & Osterbrock 1987; Baldwin et al. 1981). Hence, they are closer to the sequence of star-forming galaxies on

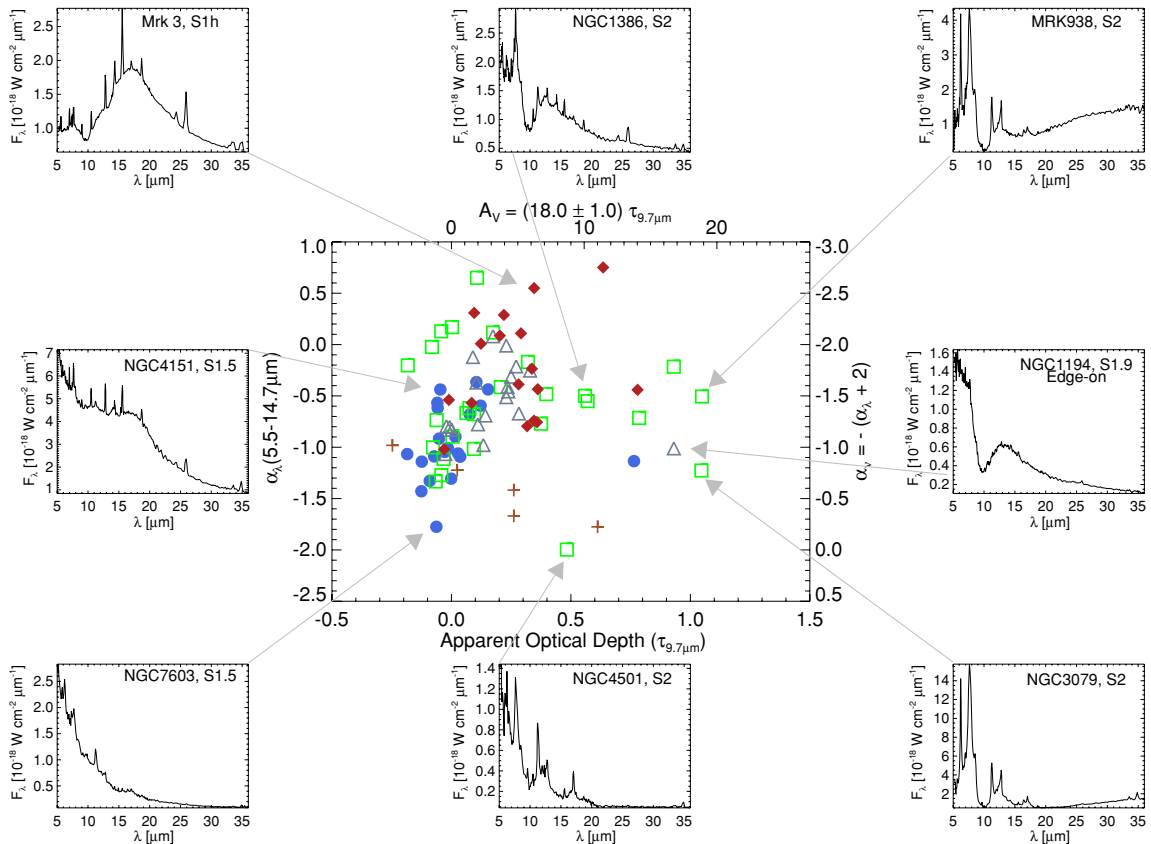


Figure 7. Effect of host galaxy dust on mid-IR spectra of AGN—central plot shows the variation of $\alpha_{\lambda}(5.5-14.7 \mu\text{m})$ with $\tau_{9.7 \mu\text{m}}$; left panels: spectra of AGN-dominated galaxies; middle panels: increasing cold dust and PAH contribution attributed to star formation in the host galaxy; right panels: Inclined host galaxies without strong PAH features (NGC 1194) or with strong PAH features (Mrk 938 and NGC 3079). Essentially, in all systems with $\tau_{9.7 \mu\text{m}} \gtrsim 0.4$ the apparent optical depth at $9.7 \mu\text{m}$ is likely due to cold dust in the host galaxy. In the panels, from left to right, star formation contribution increases.

(A color version of this figure is available in the online journal.)

the BPT diagram. The term “non-HBLR” does not imply a lack of the BLR, but that it is not detected in the observations that lead to their classification as S2. For example, Mrk 573 was originally classified as a non-HBLR. It has been shown to contain a HBLR by Nagao et al. (2004) with higher signal-to-noise observations. Further work by Lumsden et al. (2004) and Haas et al. (2007) suggests that non-HBLR objects are weak AGNs with a dominant host galaxy component. Their mid-IR spectra should then be dominated by star-forming features within the host galaxies, which is what we find here.

Five out of the 16 HBLR Seyferts that we added to our original sample show the enhanced emission bump around 15–20 μm and the rest show power-law-like mid-IR continua similar to most Seyfert 1s. One out of 16 shows strong PAH bands, and all of them have moderately strong 10 μm silicate absorption features. Thus, our comparison here provides qualitative agreement with the picture of non-HBLRs as weak AGNs with a strong starburst component. Since we have complete mid-IR spectra, we can quantify starburst and AGN contributions over the whole IRS spectral range.

5. STARBURST CONTRIBUTION IN SEYFERT GALAXIES

Many studies have explored the question of separating starburst contribution from AGN contribution using different diagnostics. Genzel et al. (1998) compared the strength of 7.7 μm PAH to [O IV] 25.89 μm /[Ne II] 12.81 μm emission line ratio, to study the AGN contribution in ultra-luminous infrared galaxies (ULIRGs). Laurent et al. (2000) used spectral templates of H II regions, photo-dissociation regions and AGNs to construct diagnostic diagrams. Sturm et al. (2002) suggested use of emission lines and continuum diagnostics. Meléndez et al. (2008a) used estimate of [Ne II] from pure AGN sources to constrain AGN and starburst fraction in a sample of Seyfert galaxies. Nardini et al. (2008) used templates for starburst and AGN components in the 5–8 μm region to estimate relative strengths in ULIRGs.

In Deo et al. (2007), we noted that the equivalent width of 6.2 μm PAH increases as $\alpha_\lambda(20\text{--}30\text{ }\mu\text{m})$ became more positive, which suggested that this relation was driven by the starburst content of the active galaxy. In Figure 3, we find that most Seyfert 1.8/1.9 and Seyfert 2 galaxies dominated by PAH emission have positive $\alpha_\lambda(20\text{--}30\text{ }\mu\text{m})$. To measure the contribution of starburst features to individual galaxies on this diagram, we use the average starburst galaxy spectrum from Brandl et al. (2006). We assume that the PAH inter-band ratios in this average spectrum are representative of typical PAH inter-band ratios in starburst galaxies. We are aware that PAH inter-band ratios can be different within different star-forming template spectra (e.g., Peeters et al. 2004; Smith et al. 2007b), and depend particularly on the strength of the starburst ionization field. Further, Sturm et al. (2006) also show that PAH ratios can be different in LINER spectra. We find similar variations in our Seyfert spectra also. We note that the strength of the 6.2, 7.7, and 8.6 μm PAH complexes vary much more than others. As a first-order comparison, assuming a fixed PAH template is acceptable. We also assume that the contribution of cool dust to the long-wavelength continuum in this average spectrum is typical of star-forming galaxies. This simple subtraction of a scaled starburst template assumes that any obscuration in the object is entirely due to the torus and not due to the surrounding starburst. We normalize the template starburst spectrum, so that the peak flux density of the 6.22 μm PAH band is unity. Then, we scale and subtract this template

by trial and error from the Seyfert spectra. We require that the 17 μm PAH complex and the 11.3 μm PAH bands be cleanly subtracted. Figure 8 shows examples of such subtractions.

Out of 107 sources for which we performed the starburst subtraction, 50 show power-law-like continuum over the whole IRS range with weak silicate emission features, after the subtraction. Twenty four objects show silicate absorption at 10 μm . Seven objects show strong silicate emission features with $f_{10\text{ }\mu\text{m}} > f_{18\text{ }\mu\text{m}}$ and an underlying power-law-like continuum. We find 26 objects where the 15–20 μm emission is much more prominent than the 10 μm emission.

The majority of Seyfert galaxies in this sample show similar PAH inter-band ratios as in the starburst template spectrum. However, in a few cases like Mrk 477 in Figure 8, we find that the PAH 6.2 and 7.7 μm bands are over-subtracted. This indicates that PAH inter-band ratios in AGN spectra are not always similar to those in starburst galaxies. Assuming that the 11.3 μm and 17 μm bands represent the actual strength of the starburst in these sources, we find a deficit of emission at 6.2 and 7.7 μm PAH bands in some Seyfert galaxies. On the other hand, in sources clearly dominated by starburst contribution such as Mrk 938 and NGC 3079, we find an excess of emission at 6.2 and 7.7 μm , after PAH bands at 11.3 and 17 μm are cleanly subtracted. We note that the over-subtraction of PAH 6.2 and 7.7 μm bands occurs in Seyfert galaxies with weak short-wavelength mid-IR continua. These variations in PAH ratios are interesting, as relating the change in PAH inter-band ratios with the decreasing intensity of the interstellar radiation field over time, as the starburst fades, will provide crucial constraints on the time required for the active nucleus to become recognizable after the starburst episode.

The starburst subtraction process essentially yields the AGN spectrum devoid of any star-forming features. These starburst-subtracted spectra are shown in Figure 9. It is instructive to compare this figure with Figure 1. Note the striking similarity of mid-IR active nuclear continua between all Seyfert optical subtypes. Type 1 spectra are flatter at short wavelengths than type 2 and type 1.8/1.9 spectra. Emission lines are generally weaker in PAH-dominated Seyfert 2s and Seyfert 1.8/1.9s (see Figure 1) suggesting weaker active nuclear continua (Deo et al. 2007; Meléndez et al. 2008b).

We measure the contribution from the starburst-subtracted AGN spectrum at continuum wavelengths of 5.5, 8, 10, 14.7, 20, and 30 μm . In Figure 10, we plot the luminosity density at 5.5 and 20 μm from the active nucleus and the starburst component. Starburst contributions at 10, 1, 0.1, 0.01, and 0.001 times the active nucleus contribution are also shown with thin lines. The starburst-to-active nuclear continuum ratios are given in Table 3 for reference. The galaxies with strong PAH bands (almost all Seyfert 1.8/1.9s and some Seyfert 2s with undetected polarized broad lines) indeed have starburst luminosities almost as much as their active nucleus contribution, but not larger at this wavelength. The sample as a whole is weighted toward significant contribution (\sim factor of 10) from the active nucleus component at 5.5 μm . Figure 10 (right) also shows similar comparison at 20 μm . This figure shows that the AGN contribution decreases rapidly at longer wavelengths. Around \sim 20 μm , the starburst and the active nuclear contribution are similar. This validates our use of $\alpha_\lambda(20\text{--}30\text{ }\mu\text{m})$ in Figure 3 to separate objects dominated by starburst contribution.

We construct spectral indices, as previously described in Section 3, from these starburst-subtracted spectra. In

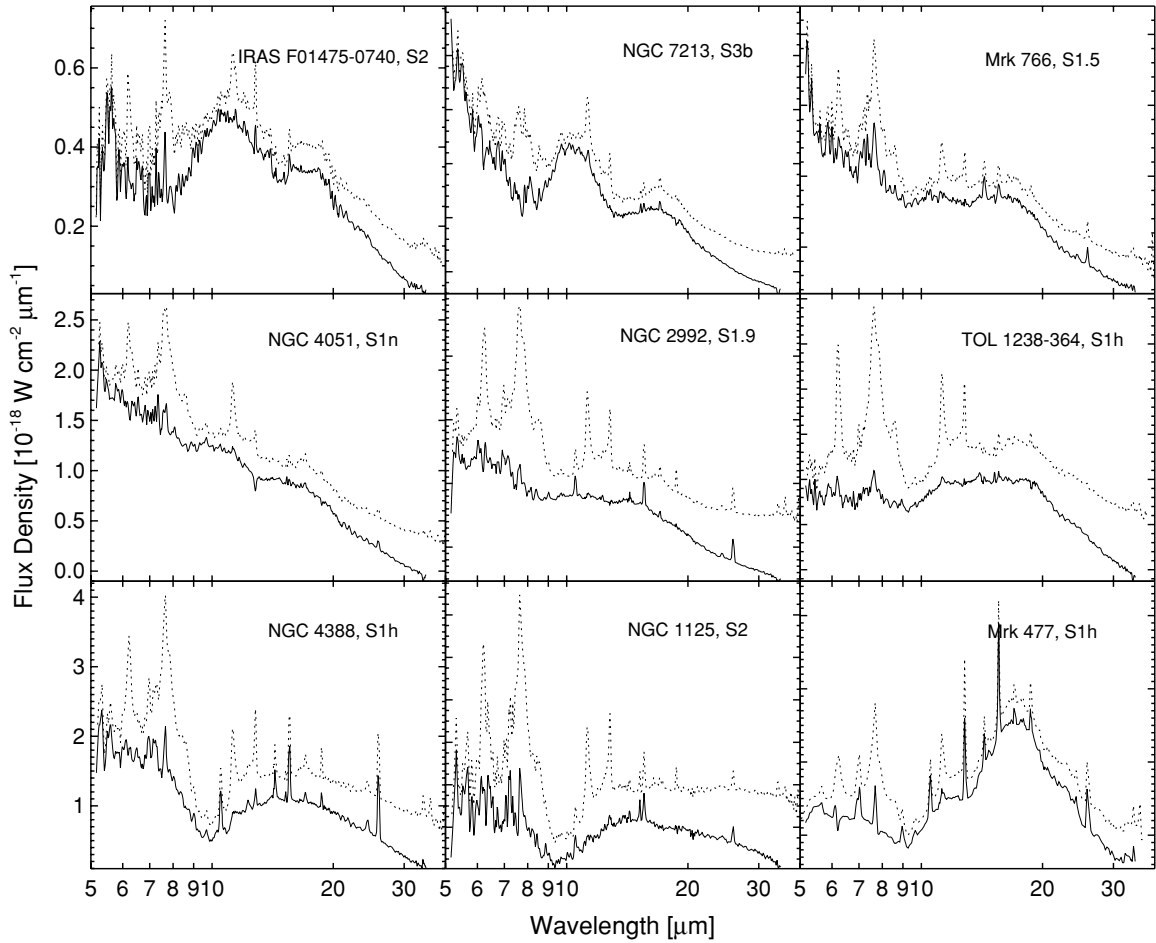


Figure 8. Seyfert spectra after subtraction of starburst components: the dotted line shows the observed spectrum and the solid line shows the subtraction of an average starburst template from this spectrum. See Figure 1 in Deo et al. (2007) for identification of emission lines and PAH bands in mid-IR spectra. Note the clearly visible silicate features, the power-law-like shape of the 5–8 μm continuum and the 15–20 μm bump. In most cases, the 7.65 μm [Ne VI] lines are also cleanly separated.

Section 3, we could not use the 8 μm flux density to construct $\alpha_\lambda(5.5\text{--}8.0\text{ }\mu\text{m})$ due to the contribution of the 7.7 and 8.6 μm PAH bands. With the starburst-subtracted spectra this is now possible. A comparison of $\alpha_\lambda(5.5\text{--}8.0\text{ }\mu\text{m})$ with $\alpha_\lambda(20\text{--}30\text{ }\mu\text{m})$ shows that the long-wavelength continua are now flatter after subtraction of the starburst component (see Figure 11, top). We find that $\langle\alpha_\lambda(5.5\text{--}8\text{ }\mu\text{m})\rangle = -0.73 \pm 0.07$ and $\langle\alpha_\lambda(20\text{--}30\text{ }\mu\text{m})\rangle = -2.05 \pm 0.10$. For comparison, the average values for these quantities in Figure 3 are -0.66 ± 0.06 and -1.04 ± 0.10 , respectively. There is clearly a large change in $\alpha_\lambda(20\text{--}30\text{ }\mu\text{m})$, confirming our conclusion again from last paragraph. The main effect of subtracting the starburst template spectrum is to shift the PAH-dominated Seyfert 1.8/1.9s and Seyfert 2s to the left. Note that there are no Seyferts with $\alpha_\lambda(20\text{--}30\text{ }\mu\text{m}) > -0.5$ in the bottom right quadrant now, which proves our earlier point (see Section 3) about PAH contamination at 5.5 μm . Figure 11 (top) shows that there are at least two types of dust distributions in the active nuclear region, one that generates the short-wavelength continua and other that generates the long-wavelength continua. The major difference between these two dust distributions is likely of their mean temperatures. By subtracting the starburst and associated cool dust contribution, we have essentially removed the starburst component that contributes most to the variety of Seyfert spectra (Buchanan et al. 2006).

A comparison of $\alpha_\lambda(5.5\text{--}8\text{ }\mu\text{m})$ against luminosity density at 5.5 μm (Figure 11, bottom) shows that Seyfert 1s have

$\langle\alpha_\lambda(5.5\text{--}8\text{ }\mu\text{m})\rangle = -1.13 \pm 0.08$, while Seyfert 2s (type S1h, S1.8, S1.9, and S2) have $\langle\alpha_\lambda(5.5\text{--}8\text{ }\mu\text{m})\rangle = -0.49 \pm 0.07$. A Kolmogorov–Smirnov test of the two distributions gives a probability of 4.42×10^{-5} of null hypothesis that the two samples are drawn from the same distribution. The value of $\alpha_\lambda(5.5\text{--}8\text{ }\mu\text{m})$ for Seyfert 1s is in agreement with estimates derived for type 1 quasars (Gallagher et al. 2007; Haas et al. 2003).

6. SUMMARY

An analysis of archival *Spitzer Space Telescope* mid-IR spectra of Seyfert galaxies is presented. We focus on understanding the intrinsic shape of the active nuclear continuum in the mid-IR region and how it relates to other properties of the source such as the 10 μm silicate optical depth. We assumed a template spectrum for the starburst component, and subtracted it from the Seyfert spectra to separate the active nuclear contribution from the circum-nuclear starburst contribution. Our primary conclusions from this study are as follows.

1. Seyfert spectra are classified effectively between AGN- and starburst-dominated categories based on the spectral indices, $\alpha_\lambda(5.5\text{--}14.7\text{ }\mu\text{m})$ and $\alpha_\lambda(20\text{--}30\text{ }\mu\text{m})$ (see Figure 3). Seyferts dominated by the AGN contribution have flatter spectra with $\alpha_\lambda(5.5\text{--}14.7\text{ }\mu\text{m}) \sim -1.13$. The added starburst contribution from the host galaxy in the large *Spitzer* aperture (see Table 1) makes $\alpha_\lambda(20.0\text{--}30.0\text{ }\mu\text{m})$ more

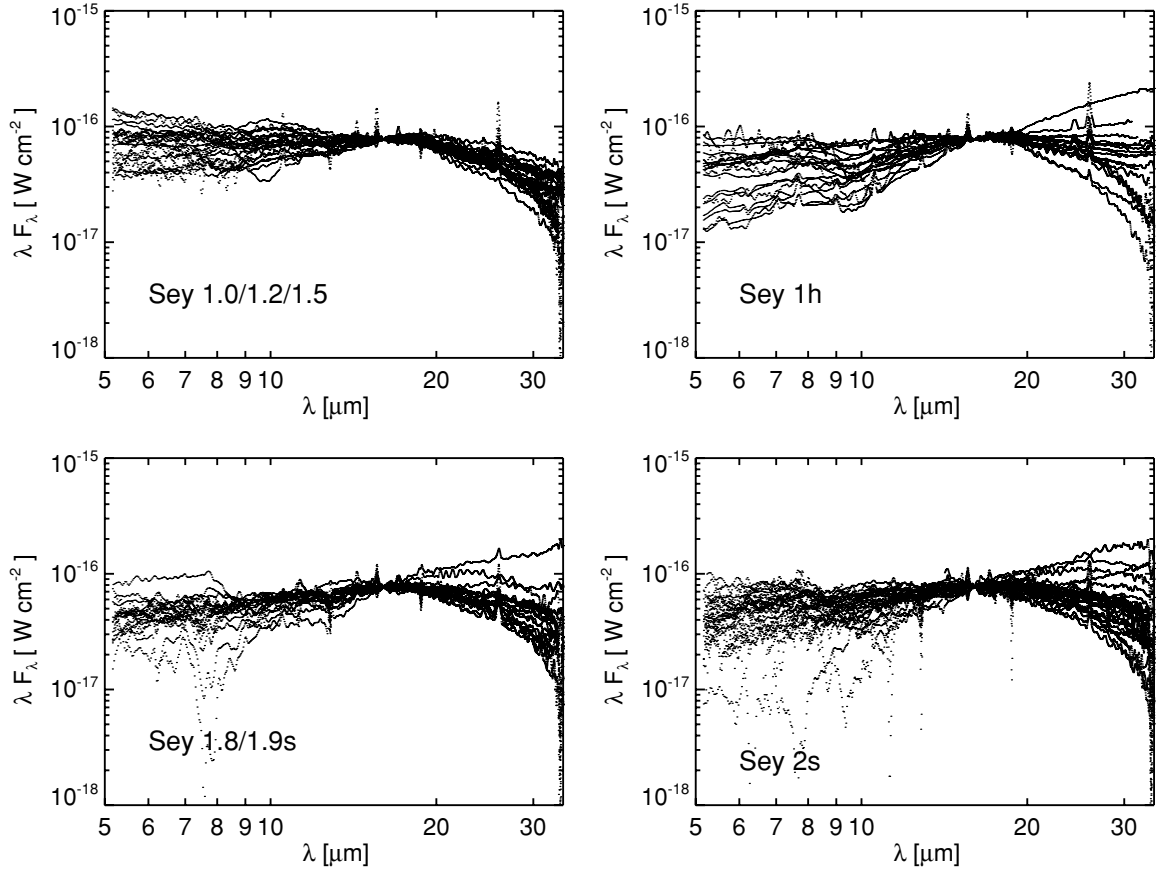


Figure 9. Mid-infrared spectra from Figure 1 after subtraction of a scaled starburst template spectrum. The spectra are normalized at $14.7 \mu\text{m}$. Top left: Seyfert 1s; top right: Seyfert 2s with evidence of broad optical emission lines in polarized light; bottom left: Seyfert 1.8/1.9s; bottom right: Seyfert 2s with undetected polarized broad emission lines. Compare this figure with Figure 1. On average, after starburst subtraction, PAH-dominated Seyfert 1.8/1.9s and Seyfert 2s show similar continuum shapes as type 2 Seyferts with HBLR (top right panel). There is a striking similarity in the active nuclear continuum of all Seyfert types beyond $\sim 15 \mu\text{m}$.

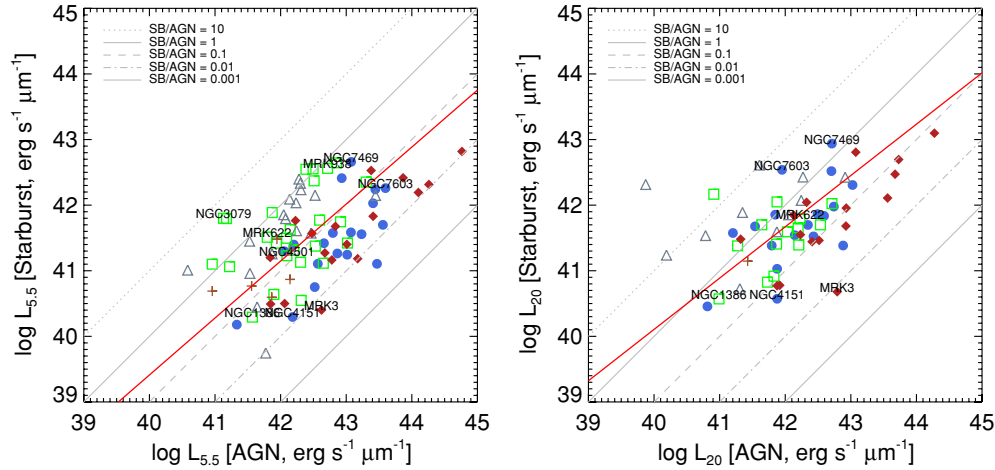


Figure 10. Luminosity density at $5.5 \mu\text{m}$ (left) and $20 \mu\text{m}$ (right) from the starburst and the active nuclear components. Our sample shows a strong contribution from the active nuclear component, and galaxies with large starburst contributions are preferentially Seyfert 1.8/1.9s and some Seyfert 2s with unidentified broad polarized emission lines. The thick red line shows a linear regression fit (bisector method) to data points. The diagonal lines show starburst-to-AGN contribution ratio. Symbols for Seyfert types are same as in Figure 3. At longer wavelengths, the average starburst fraction increases and is roughly the same as the AGN contribution at $\sim 20 \mu\text{m}$. (A color version of this figure is available in the online journal.)

positive or steeper. A key property that distinguishes AGN-dominated spectra is that the $20\text{--}30 \mu\text{m}$ continuum is flatter ($\alpha_\lambda \sim -2$) than the very steep $20\text{--}30 \mu\text{m}$ continuum of starburst-dominated objects ($\alpha_\lambda \sim 1$). The $20\text{--}30 \mu\text{m}$ continuum is likely formed from the Rayleigh–Jean’s tail of the “warm” dust component. It is likely that there are multiple

“warm” components with different temperatures. Further, Type 2 Seyferts with polarized broad emission lines in their optical spectra (type S1h) show $\alpha_\lambda(5.5\text{--}14.7 \mu\text{m}) \sim -0.49$ much different than average type 1 Seyferts that show $\alpha_\lambda(5.5\text{--}14.7 \mu\text{m}) \sim -1.13$. Note the steeper and weak short-wavelength continuum in Figure 9, as compared to

Table 3
Starburst-to-AGN Flux Density Ratios

Galaxy Name (1)	Starburst-to-AGN Flux Density Ratio				
	5.5 μm (2)	10 μm (3)	14.7 μm (4)	20 μm (5)	30 μm (6)
3C 321	0.0263	0.0400	0.0207	0.0354	0.0640
CGCG 381-051	...	0.2681	0.5661	0.9087	...
ESO 12-G21	0.3020	0.7335	13.4681
ESO 33-G2	0.0291	0.0359	0.0622	0.1534	0.9593
IC 4329A	0.0043	0.0082	0.0145	0.0317	0.1481
IRAS 05189-2524	0.0355	0.0640	0.0610	0.0925	0.1097
IRASF 01475-0740	0.0702	0.0835	0.1556	0.2870	1.7003
IRASF 04385-0828	0.0253	0.0887	0.0715	0.1456	0.4536
IRASF 15480-0344	0.0679	0.0696	0.1084	0.2052	0.9631
MCG+0-29-23	1.4460	11.5036
MCG-03-34-064	0.0247	0.0309	0.0323	0.0571	0.1434
MCG-2-33-34	0.1739	0.3531	0.6773	2.3617	...
MCG-2-40-4	0.0613	0.1260	0.2427	0.6416	17.9313
MCG-3-34-63	0.3026	38.4053
MCG-3-58-7	0.0501	0.0891	0.1635	0.3254	1.5569
MCG-5-13-17	0.1574	0.3035	0.5114	1.3713	...
MCG-6-30-15	0.0171	0.0288	0.0588	0.1249	0.6378
Mrk 1239	0.0138	0.0281	0.0706	0.1727	1.1758
Mrk 3	0.0060	0.0077	0.0051	0.0077	0.0233
Mrk 334	0.4212	0.6677	1.0960	1.4361	4.5979
Mrk 348	0.0395	0.0754	0.0971	0.2081	1.8993
Mrk 463E	0.0124	0.0329	0.0364	0.0627	0.1964
Mrk 471	0.6422	1.7036
Mrk 477	0.0695	0.0817	0.0705	0.1061	0.2781
Mrk 6	0.0170	0.0411	0.0668	0.1237	0.6543
Mrk 609	1.3144	2.3839	25.1028
Mrk 622	0.5186	0.3268	0.3328	0.3661	0.7087
Mrk 766	0.0574	0.0914	0.1203	0.2250	0.7952
Mrk 79	0.0211	0.0429	0.0809	0.1754	0.7295
Mrk 817	0.0417	0.0625	0.1186	0.1911	0.6321
Mrk 883	0.5226	0.8595	0.7567	0.6741	1.1640
Mrk 9	0.0627	0.0951	0.2400	0.6527	...
Mrk 938	0.7001	...	6.2222	...	11.4720
NGC 1125	0.3060	1.8193	0.6179	1.1437	4.2422
NGC 1143/4	0.6227
NGC 1241	0.2527	1.2900	3.9115
NGC 1320	0.0667	0.0964	0.1615	0.3454	2.5940
NGC 1365	0.8418	3.5882	2280.9476
NGC 1386	0.0528	0.1621	0.1460	0.3804	1.4503
NGC 2273	0.2300	0.4914	0.5444	1.4474	88.6744
NGC 2622	0.1445	0.2242	0.2628	0.5276	13.8732
NGC 2639	0.3437	31.3315
NGC 2992	0.2337	0.4174	0.6511	3.4637	...
NGC 3079	4.6747
NGC 3081	0.0442	0.0485	0.0480	0.0785	0.2137
NGC 3227	0.4713	0.9641	...
NGC 3511	2.6708
NGC 3516	0.0170	0.0389	0.0758	0.1423	0.5974
NGC 3660	...	1.1048
NGC 3786	0.2673	0.6172	1.4630	11.1716	...
NGC 3982	2.6710	9.3812
NGC 4051	0.0702	0.1056	0.1872	0.4395	7.1327
NGC 4151	0.0129	0.0186	0.0263	0.0497	0.2452
NGC 424	0.0102	0.0200	0.0390	0.0885	0.5310
NGC 4388	0.1237	0.5162	0.3060	0.5262	2.9754
NGC 4501	0.1361	1.2925
NGC 4507	0.0242	0.0372	0.0588	0.1080	0.3233
NGC 4579	0.0539	0.1936
NGC 4593	0.0346	0.0630	0.1552	0.3887	3.2523
NGC 4594	0.0094	0.0609
NGC 4602	0.8372	2.8868
NGC 4922 NED01	0.1114	0.2474
NGC 4941	0.8976	1.4715	...
NGC 4968	0.1301	0.1651	0.1894	0.3638	4.7134

Table 3
(Continued)

Galaxy Name (1)	Starburst-to-AGN Flux Density Ratio				
	5.5 μm (2)	10 μm (3)	14.7 μm (4)	20 μm (5)	30 μm (6)
NGC 5005	0.1619	2.3674
NGC 513	0.9011	1.1506
NGC 5135	0.7242	3.4740	8.6441
NGC 5256 NED01	1.1450	65.3742	8.9031
NGC 5347	0.0552	0.0598	0.0665	0.1229	0.5838
NGC 5506	0.0250	0.1339	0.1109	0.2495	0.9290
NGC 5929	0.5391
NGC 5953	4.1648
NGC 6810	1.0366	1.9786	4.2739	17.9650	...
NGC 6860	0.0602	0.1206	0.3297	1.0168	...
NGC 6890	0.2445	0.4524	0.9600	5.6312	...
NGC 7130	1.0761	2.3340	2.4662	10.1020	...
NGC 7213	0.0530	0.0914	0.2545	0.5246	...
NGC 7314	0.4652	1.9107	...
NGC 7469	0.3845	0.5837	0.9244	1.6895	...
NGC 7496	1.3900	1.0345	0.9555	1.2744	3.7034
NGC 7582	0.3118	9.1000	2.2330	536.9538	...
NGC 7590	0.6934
NGC 7603	0.0458	0.1133	0.4841	3.8650	...
NGC 7674	0.1407	0.2002	0.2614	0.5388	7.2992
NGC 788	0.0274	0.0361	0.0380	0.0728	0.2437
NGC 931	0.0326	0.0600	0.1093	0.2347	1.4468
SDSS J1039+6430	0.0114	0.0188	0.0268
TOL 1238-364	0.3450	0.3095	0.3202	0.5216	8.6584
UGC 11680 NED01	0.1504	0.1820	0.4536	1.4949	...
UGC 12138	0.1290	0.2047	0.3179	0.6320	3.1993
UGC 7064	0.6323	0.4803	1.2807	276.5345	...
UM 146	0.0639	0.1100	0.1527	0.2621	0.5764
WIR-IRAS 23060+0505	0.0113	0.0248	0.0338	0.0665	0.1457

Notes. Col. (1): Galaxy name; Cols. (2–6): Starburst-to-AGN flux density ratio measured at 5.5, 10, 14.7, 20, and 30 μm ; a missing ratio implies either the spectrum was incomplete at that wavelength or the AGN contribution was negative after starburst subtraction. A very large ratio indicates very weak AGN contribution, these typically occur at or beyond 14.7 μm in a few galaxies. See Figure 10 for a visual representation of these ratios, and Table 1 for aperture size in parsecs. Even in nearby AGN, *Spitzer* spectra sample regions of size ~ 1 kpc. See Section 5 for discussion of the starburst subtraction process and results.

- type 1 Seyferts. This is a direct evidence for presence of the dust torus that blocks our view of the hot dust closer in.
- After starburst subtraction, Seyfert 1.8/1.9s and Seyfert 2s with strong PAH features in their spectra show similar active nuclear continuum as Seyfert 2s with weak/absent PAH features in their mid-IR spectra and polarized broad emission lines in their optical spectra (see Figure 9). This suggests presence of similar quantities and/or properties of dusty material around the central accretion disk in these type 2 sources. Tran (2003) had proposed existence of two types of Seyfert 2s: the HBLR and the non-HBLRs. We compared spectral indices in the 5–8 μm region after starburst subtraction and find that both the HBLR and non-HBLR show similar spectral indices (Figure 11, bottom), suggesting similarity rather than differences between the two classifications. While, non-HBLRs tend to show stronger starburst contribution as compared to their AGN contribution, the converse (that starburst-dominated systems lack BLR signatures) is not necessarily true. The additional host galaxy contribution likely complicates the identification of BLR in these systems. As we show in Figure 3, simple continuum indices effectively separate AGN-dominated Seyferts from starburst-dominated Seyferts in the mid-IR.
 - Deo et al. (2007) showed that a large part of the silicate absorption in some Seyfert galaxies comes from starburst-heated cold dust in the host galaxy rather than the dust

- torus. This conclusion was based on the fact that only highly inclined galaxies showed large silicate optical depths. Here, we put that result on a better statistical basis by presenting a correlation between the b/a and the measured optical depth for this sample of 109 sources (see Figure 6). All objects with significant optical depth are highly inclined and are also classified as Seyfert 2s or Seyfert 1.8/1.9s. This confirms previous results by Keel (1980) and Maiolino & Rieke (1995), and highlights the importance of considering the host galaxy contribution in concealing AGNs.
- On average, Seyfert galaxies dominated by the AGN continuum tend to show weak silicate absorption ($\tau_{9.7} \lesssim 0.4$). The short-wavelength continuum index ($\alpha_\lambda(5.5\text{--}14.7 \mu\text{m})$) and the apparent silicate optical depth $\tau_{9.7}$ (Figure 4) may be correlated in AGN-dominated objects. Seyfert optical types form a continuous sequence of increasing optical depth along this correlation from type 1s, type 1.8/1.9s, to type 2s with HBLRs. This validates the general inclination dependence inherent in AGN models noted before in the mid-IR by Hao et al. (2007). But, as can be noted in Figure 4, there is not a strict relationship between the strength of silicate features and the optical spectral type.
 - Figure 11 (top) shows that there are at least two types of dust distributions in the active nuclear region, one that generates the short-wavelength continua and another that generates the long-wavelength continua. The major difference

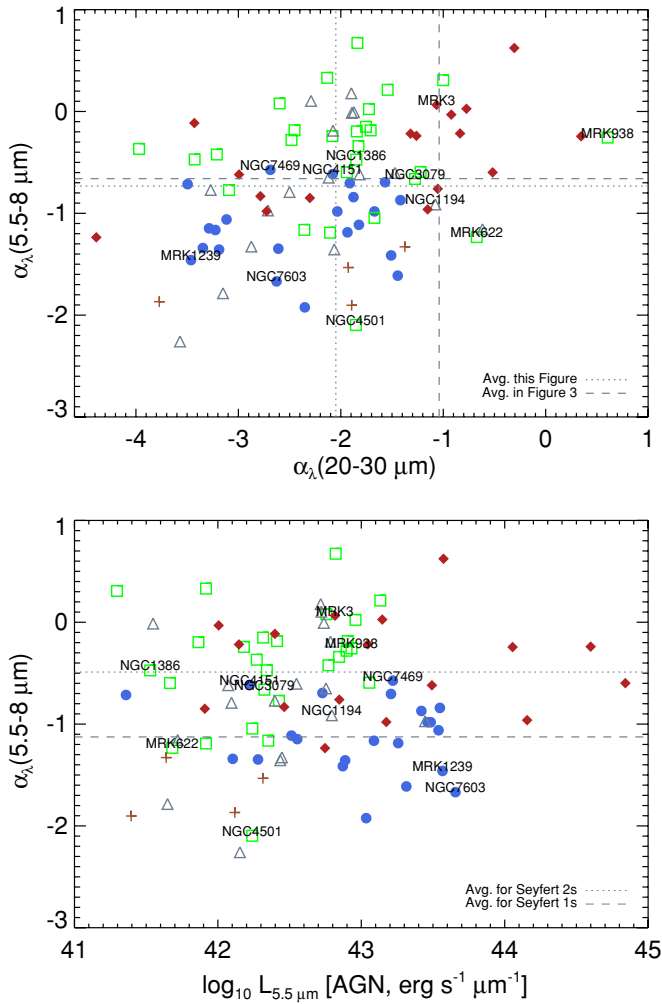


Figure 11. Top: comparison between $\alpha_\lambda(5.5-8.0 \mu\text{m})$ and $\alpha_\lambda(20-30 \mu\text{m})$ after subtraction of starburst component. $\alpha_\lambda(20-30 \mu\text{m})$ values are more negative than in Figure 3 (dashed lines), indicating flatter continua than those at short wavelength. Bottom: wavelength spectral index between 5.5 and $8 \mu\text{m}$ after starburst subtraction compared to the luminosity density of the AGN component at $5.5 \mu\text{m}$. The dashed line shows the average spectral index for Seyfert 1 galaxies, and the dot-dashed line shows the average spectral index for Seyfert 2 (including S1h) and Seyfert 1.8/1.9 galaxies. Symbols for Seyfert types are same as in Figure 3.

(A color version of this figure is available in the online journal.)

between these two dust distributions is likely of their mean temperatures. By subtracting the starburst and associated cool dust contribution, we have essentially removed the starburst component that contributes most to the variety in Seyfert spectra (Buchanan et al. 2006). In Figure 2, we demonstrate the existence of this “warm” component which dominates the long-wavelength continuum, by separating it from the hot dust component in Mrk 766. This simple template subtraction exercise provides proof that Seyfert spectra are primarily thermal in nature and composed of at least three thermal components with $T \sim 1000$, 200, and 60 K. The reported “break” in the spectrum at $\sim 20 \mu\text{m}$ in type 1 Seyfert spectra is a result of this warm component being brighter at $\sim 20 \mu\text{m}$ than the Rayleigh–Jean’s tail of the hot component. The above-mentioned similarity of continua beyond $\sim 15 \mu\text{m}$ in AGN-dominated sources is also due to this warm dust component being present in almost all observed AGN spectra.

We would like to thank Nadia Zakamska for insightful comments on an early draft of this paper. G.T.R. acknowledges support from an Alfred P. Sloan Research Fellowship. This work is based on archival data obtained with the *Spitzer Space Telescope*, which is operated by the Jet Propulsion Laboratory, California Institute of Technology under a contract with NASA. This research has made use of the NASA/IPAC Extragalactic Database (NED) which is operated by the Jet Propulsion Laboratory, California Institute of Technology, under contract with the National Aeronautics and Space Administration. This research has also made use of NASA’s Astrophysics Data System Bibliographic Services. The IRS was a collaborative venture between Cornell University and Ball Aerospace Corporation funded by NASA through the Jet Propulsion Laboratory and Ames Research Center. SMART was developed at Cornell University and is available through the Spitzer Science Center at Caltech.

Facility: *Spitzer*

REFERENCES

- Alonso-Herrero, A., Quillen, A. C., Simpson, C., Efstathiou, A., & Ward, M. J. 2001, *AJ*, **121**, 1369
- Antonucci, R. 1993, *ARA&A*, **31**, 473
- Antonucci, R. R. J., & Miller, J. S. 1985, *ApJ*, **297**, 621
- Baldwin, J. A., Phillips, M. M., & Terlevich, R. 1981, *PASP*, **93**, 5
- Brandl, B. R., et al. 2006, *ApJ*, **653**, 1129
- Buchanan, C. L., Gallimore, J. F., O’Dea, C. P., Baum, S. A., Axon, D. J., Robinson, A., Elitzur, M., & Elvis, M. 2006, *AJ*, **132**, 401
- Clavel, J., et al. 2000, *A&A*, **357**, 839
- Deo, R. P., Crenshaw, D. M., Kraemer, S. B., Dietrich, M., Elitzur, M., Teplitz, H., & Turner, T. J. 2007, *ApJ*, **671**, 124
- Edelson, R. A., & Malkan, M. A. 1986, *ApJ*, **308**, 59
- Gallagher, S. C., Richards, G. T., Lacy, M., Hines, D. C., Elitzur, M., & Storrie-Lombardi, L. J. 2007, *ApJ*, **661**, 30
- Genzel, R., et al. 1998, *ApJ*, **498**, 579
- Haas, M., Siebenmorgen, R., Pantin, E., Horst, H., Smette, A., Käufel, H.-U., Lagage, P.-O., & Chini, R. 2007, *A&A*, **473**, 369
- Haas, M., et al. 2003, *A&A*, **402**, 87
- Hao, L., Weedman, D. W., Spoon, H. W. W., Marshall, J. A., Levenson, N. A., Elitzur, M., & Houck, J. R. 2007, *ApJ*, **655**, L77
- Higdon, S. J. U., et al. 2004, *PASP*, **116**, 975
- Houck, J. R., et al. 2004, *ApJS*, **154**, 18
- Imanishi, M., & Alonso-Herrero, A. 2004, *ApJ*, **614**, 122
- Keel, W. C. 1980, *AJ*, **85**, 198
- Klaas, U., et al. 2001, *A&A*, **379**, 823
- Laurent, O., Mirabel, I. F., Charmandaris, V., Gallais, P., Madden, S. C., Sauvage, M., Vigroux, L., & Cesarsky, C. 2000, *A&A*, **359**, 887
- Lumsden, S. L., Alexander, D. M., & Hough, J. H. 2004, *MNRAS*, **348**, 1451
- Maiolino, R., & Rieke, G. H. 1995, *ApJ*, **454**, 95
- Meléndez, M., Kraemer, S. B., Schmitt, H. R., Crenshaw, D. M., Deo, R. P., Mushotzky, R. F., & Bruhweiler, F. C. 2008a, *ApJ*, **689**, 95
- Meléndez, M., et al. 2008b, *ApJ*, **682**, 94
- Mushotzky, R. F., Winter, L. M., McIntosh, D. H., & Tueller, J. 2008, *arXiv:0807.4695*
- Nagao, T., Kawabata, K. S., Murayama, T., Ohshima, Y., Taniguchi, Y., Sumiya, R., & Sasaki, S. S. 2004, *AJ*, **128**, 109
- Nardini, E., Risaliti, G., Salvati, M., Sani, E., Imanishi, M., Marconi, A., & Maiolino, R. 2008, *MNRAS*, **385**, L130
- Peeters, E., Spoon, H. W. W., & Tielens, A. G. G. M. 2004, *ApJ*, **613**, 986
- Richards, G. T., et al. 2006, *ApJS*, **166**, 470
- Rodríguez-Ardila, A., & Mazzalay, X. 2006, *MNRAS*, **367**, L57
- Rodríguez Espinosa, J. M., Pérez García, A. M., Lemke, D., & Meisenheimer, K. 1996, *A&A*, **315**, L129
- Schweitzer, M., et al. 2006, *ApJ*, **649**, 79
- Seyfert, C. K. 1943, *ApJ*, **97**, 28
- Smith, J. D. T., et al. 2007a, *PASP*, **119**, 1133
- Smith, J. D. T., et al. 2007b, *ApJ*, **656**, 770
- Spoon, H. W. W., Marshall, J. A., Houck, J. R., Elitzur, M., Hao, L., Armus, L., Brandl, B. R., & Charmandaris, V. 2007, *ApJ*, **654**, L49
- Sturm, E., Lutz, D., Verma, A., Netzer, H., Sternberg, A., Moorwood, A. F. M., Oliva, E., & Genzel, R. 2002, *A&A*, **393**, 821

- Surm, E., et al. 2006, [ApJ](#), **653**, L13
- Tommasin, S., Spinoglio, L., Malkan, M. A., Smith, H., González-Alfonso, E., & Charmandaris, V. 2008, [ApJ](#), **676**, 836
- Tran, H. D. 2001, [ApJ](#), **554**, L19
- Tran, H. D. 2003, [ApJ](#), **583**, 632
- Veilleux, S., & Osterbrock, D. E. 1987, [ApJS](#), **63**, 295
- Verma, A., Charmandaris, V., Klaas, U., Lutz, D., & Haas, M. 2005, [Space Sci. Rev.](#), **119**, 355
- Véron-Cetty, M.-P., & Véron, P. 2006, [A&A](#), **455**, 773
- Weedman, D. W., et al. 2005, [ApJ](#), **633**, 706